

Influence of the Metal Center in M-N-C Catalysts on the CO₂ Reduction Reaction on Gas Diffusion Electrodes

Stephen Paul,^{,†} Yi-Lin Kao,[‡] Lingmei Ni,^{†,§} Rayko Ehnert,[¶] Iris Herrmann-Geppert,[¶] Roel van de Krol,[‡] Robert W. Stark,[§] Wolfram Jaegermann,[§] Ulrike I. Kramm,^{*,†} and Peter Bogdanoff^{*,‡}*

[†]Department of Chemistry, TU Darmstadt, Otto-Berndt-Strasse 3, 64287 Darmstadt, Germany

[‡]Institute for Solar Fuels, Helmholtz-Zentrum Berlin für Materialien und Energie, Hahn-Meitner-Platz 1, 14109 Berlin, Germany

[¶]Faculty of Computer and Biosciences, University of Applied Sciences Mittweida, Technikumsplatz 17, 09648 Mittweida, Germany

[§]Department of Materials and Earth Sciences, TU Darmstadt, Otto-Berndt-Strasse 3, 64287 Darmstadt, Germany

Keywords

Electrocatalysis, CO₂ reduction reaction, M-N-C, M-N₄ active centers, electrochemistry coupled to mass spectrometry, CO formation, hydrocarbon formation

ABSTRACT

In this work the influences of various transition metal ions as active sites in high purity metal- and nitrogen-doped carbon catalysts (in short M-N-C, where M: Mn³⁺, Fe³⁺, Co²⁺, Ni²⁺, Cu²⁺, Zn²⁺, Sn⁴⁺ in the catalyst powders), were systematically investigated for the electrochemical reduction of CO₂ in aqueous electrolyte. The practically sole presence of M-N₄ centers as catalytic sites was determined by X-ray photoelectron spectroscopy (XPS). The catalysts were electrochemically investigated in a gas diffusion electrode arrangement in bypass mode coupled in-line to a mass spectrometer, which allowed the almost simultaneous detection of potential-dependent product selectivities, faradaic efficiencies and current densities in linear sweep voltammetry experiments. *Post mortem* XPS analysis was performed after different stages of operation on the Cu-N-C catalyst, which was the only catalyst to produce hydrocarbons (CH₄, C₂H₄) in significant amounts. Here, we provide insights on the potential-induced electronic changes of the Cu-N-C catalyst occurring under operating conditions. Our work further experimentally reveals the high affinity of M-N-C catalysts to convert CO₂ to industrially relevant carbonaceous raw materials while widely suppressing the competing hydrogen evolution reaction. These discoveries lead to a better understanding of the role of the active sites, specially the central metal ion, in M-N-C and could contribute significantly to the improvement of selectivities and activities for the CO₂RR in this catalyst class through tailor-made optimization strategies.

1. Introduction

The steadily increasing concentration of the greenhouse gas carbon dioxide (CO₂) has a significant impact on the average temperature of the earth's atmosphere and thus the climate.¹ For this reason, measures have been taken in recent years to reduce atmospheric CO₂ emissions and concentrations.² The electrochemical co-reduction of CO₂ and water powered by electricity from renewable energy sources (e.g. photovoltaic, wind-power etc.) is a promising possibility to recycle CO₂ in an emission-neutral and energetically efficient process.^{3,4} In this way, industrially usable products such as carbon monoxide (CO), methane (CH₄) and ethene (C₂H₄), but also formic acid (HCOOH), methanol (CH₃OH) and ethanol (C₂H₅OH) can be produced.⁵⁻¹³ However, the complex reaction mechanisms still require high overpotentials and lead to different products as well as undesirable by-products. Therefore, selective and efficient electrocatalysts are required.^{14,15}

So far, metallic catalysts are the most studied materials due to their relatively high stability and high achievable current densities with regard to the electrochemical CO₂ reduction reaction (CO₂RR). Improving the stability and product selectivity of metallic catalysts for technical applications is one of the subjects of current research.¹⁶⁻¹⁸ In addition, molecular catalysts, which are mostly based on metal-organic molecules and macrocycles immobilized on conductive substrates, are subject to intensive investigations.¹⁹⁻²⁸ A detailed overview on molecular catalysts is given by the perspective of Thorbensen et al. (2020) and the review papers of Varela et al. (2018) and Takeda et al. (2017).²⁹⁻³¹ Due to the very defined bond formation between CO₂ and the single site molecular catalytic centers, high selectivities with regard to a desired product were achieved during electrolysis. However, these catalysts still show limited stability, low current densities and poor production rates under operating conditions in comparison to metallic catalysts.³²⁻³⁷

Low cost carbon-based materials represent a relatively new and yet little-investigated catalytic approach for the co-electrolysis of CO₂ and water. In addition to solid Metal Organic Frameworks (MOFs) and nitrogen-doped carbons (N-C), metal- and nitrogen-doped carbon catalysts (M-N-C) were also found to be active towards the CO₂RR.^{19,38-49} Within this catalyst class, the most active site is identified as a single base transition metal ion that is coordinated to nitrogen atoms as M-N_x centers which are integrated in to graphene layers of the carbon matrix.⁴⁹ A schematic representation of one possible model for a M-N₄ center is visualized in **Figure 1**. With its delocalized electrons, graphene does not only serve as an inorganic, highly conductive carrier for the M-N_x centers, but also as an electron pool, which interacts with the center and might influence the entire catalytic process with its variable electronic and chemical properties. This class of M-N-C materials therefore has structures and properties that can be classified between inorganic and molecular catalysts. M-N-C catalysts were originally developed for the electrochemical oxygen reduction reaction (ORR).⁵⁰⁻⁵⁵ From this research it is known, that they can easily be produced by pyrolyzing a metal-salt or -macrocycle in the presence of nitrogen and carbon containing precursors.

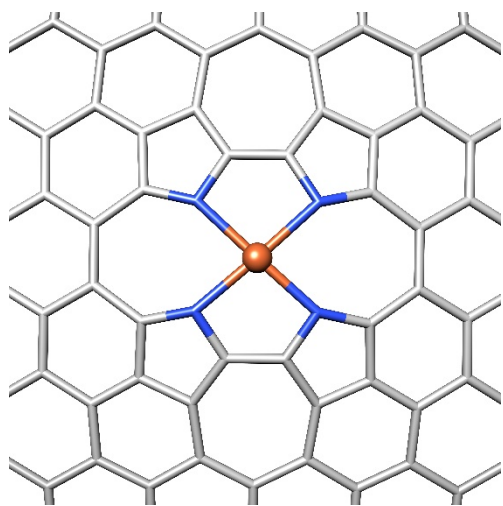


Figure 1. Exemplary structural scheme of a M-N₄ center in M-N-C catalysts. In this scheme the central metal ion (orange) is coordinated to four pyrrolic nitrogen atoms (blue), embedded in a graphene-like carbon matrix (grey).

Even though not all details about these catalysts have been clarified, especially the M-N₄ centers are assumed to be the active sites.^{19,25} Theoretical calculations predict that these “single metal atom” centers, can significantly suppress the competing hydrogen evolution reaction (HER) compared to metallic interfaces and thus increase the selectivity for the CO₂RR.¹⁹ This was substantiated experimentally, since Fe- and Ni-nanoparticles almost predominantly show HER, while Fe-N-C and Ni-N-C catalysts predominantly reduce CO₂ to CO.^{39,56}

Furthermore, numerous experimental and theoretical investigations show that the type of metal ion in the catalytic center has a decisive role concerning selectivity and activity in the CO₂RR.^{30,49} However, a direct comparison of these published results is often difficult, since different preparation methods lead to additional chemical structures, that can also contribute to the CO₂RR. Here, mainly pyridinic and pyrrolic nitrogen as well as metallic nanoparticles are reported, which are typically formed as by-products during preparation.^{47,51,57–60} Metal centers that are coordinated to both nitrogen and carbon are also considered to be possible active centers.⁶⁰ Finally, the molecular, electronic and microporous structure of the carbon can also have an influence on the activity and, ultimately, different experimental conditions make the comparison of the electrochemical characterizations even more difficult.⁶¹

In order to enable a meaningful comparison, the focus of our work is therefore on producing a set of catalysts that should differ preferably only in the respective metal ion of the catalytic center. Since M-N₄ centers are seen as particularly active, a preparation process is used which allows a very high proportion of M-N₄ centers without or with only few undesired by-products. This is

achieved by the pyrolysis of carbon-supported metal porphyrins under suitable conditions. The respective metal ions in the catalyst powders were: Mn^{3+} , Fe^{3+} , Co^{2+} , Ni^{2+} , Cu^{2+} , Zn^{2+} , Sn^{4+} , a metal-free reference was also investigated.

The electrocatalytic behavior of the catalysts is characterized as a drop-casted layer on commercial gas diffusion layers (GDL, Sigracet gas diffusion layer 38BC) in an electrochemical bypass gas flow cell. This allows production rates that are sufficiently large to be reliably detected via mass spectrometry (MS) almost simultaneously to the electric current measurement in linear sweep voltammetry (LSV) experiments. This advantage is rather not feasible with other widely used methods like the accumulation of products over a certain electrolysis time and the use of time consuming chromatography methods. This is especially important as there are indications that some M-N_x centers are partially reduced with increasing overpotential and electrolysis time and that therefore the product selectivity could change over time due to varying contribution of active sites.⁴¹ Interestingly, it is reported that changes in oxidation state coincided with the onset potential of hydrocarbon formation for Cu-phthalocyanine and a Cu-N-C catalyst.^{62,63} However, for their Cu-N-C Karapinar et al. possibly CO_2RR active additional nitrogen sites beside metal-bound N were shown for the as-prepared catalyst. Thus, a confirmation of this observation for M-N-C catalysts with close to exclusive M-N_4 active sites is missing. In order to get deeper insights in this unique electrochemical behaviour we conducted a thorough *post mortem* X-Ray photoelectron spectroscopy (XPS) study of our pyrolyzed Cu-N-C catalyst at different potentials.

2. Experimental section

2.1. Catalyst preparation

Porphyrins obtained from Porlab and Sigma Aldrich were used for synthesis without further purification. In **Table S1** a summary of the catalyst naming, the used porphyrins as well as their

respective weight portions and pyrolysis yields is given. The preparation is based on a well-established procedure for the synthesis of Fe-N-C catalysts with a high fraction of Fe-N₄ sites, as previously published.⁶⁴ First, 0.42 mmol of the respective (metallo-)porphyrin were dispersed in 10 ml of tetrahydrofuran (THF) in an ultrasonic bath for 5 min. Afterwards, 1 g of Ketjen Black EC-600 JD (KB600, Akzo Nobel Polymer Chemicals LLC) dispersed in 40 ml of THF were added and the mixture was ultrasonicated for 1 h. The suspension was left to rest for 12 h until most of the solvent was evaporated. Subsequently, all samples were dried at 80 °C for another 12 h. The dried precursor mixture was weighed into a quartz glass boat and placed in a quartz glass furnace. There, the respective sample was purged with N₂ for the entire pyrolysis. After 10 min of purging at room temperature the furnace was heated up to 600 °C with a heating rate of 300 °C h⁻¹, where it was kept for 1 h. The furnace was then allowed to cool down below 80 °C, before the sample was transferred into 250 ml of 2 M HCl (saturated with N₂ prior to transfer). After air-tight sealing the sample was again ultrasonicated for 1 h and left to rest for 12 h in HCl. Finally, the catalyst was filtrated and washed with approx. 2 l of ultrapure H₂O until the filtrate was pH-neutral and dried again at 80 °C for 12 h, before weighing for yield determination and further analysis. The catalysts were characterized using the following standard physico-chemical methods: N₂ gas-sorption, Raman spectroscopy and XPS. Measurement details for these characterization techniques can be found in the SI.

2.2. Preparation of the gas-diffusion electrodes (GDE)

For the catalyst ink, 200 µl of a 0.2 wt% Nafion® solution (4 µl of 5 wt% Nafion®, 98 µl ethanol, 98 µl ultrapure water) were added to 1 mg of catalyst powder (5 mg_{catalyst} ml⁻¹). The black suspension was first treated in an ultrasonic bath for 20 min and then with an ultrasonic homogenizer for 30 s. The GDE was prepared by drop-casting 50 µl of the catalyst ink

homogeneously on 0.78 cm² of a GDL, resulting in a catalyst loading of 0.32 mg cm⁻². The GDE was finally dried at 80 °C for another 20 min prior to installation into the electrochemical cell. This electrode serves as working electrode (WE) in the electrochemical cell. Due to the high similarity of our samples in XPS, N₂-sorption and Raman spectroscopy analysis (as shown in the results part), which is largely due to the usage of high amounts of KB600, and their identical processing during drop-casting, we assume that the properties of the GDE (e.g. porosity, hydrophobicity) are as similar as possible for all samples. In fact, optical contact angle measurements showed almost identical contact angles of roughly 153 ± 5° for C_i electrolyte on all GDEs (data not shown). In general, however, minor differences that could affect the measurements cannot be ruled out completely.

2.3. Electrochemical measurement setup and product analysis

The electrochemical cell was operated in a three-electrode arrangement using a PINE potentiostat. An Ag|AgCl electrode served as a reference ($E = +0.2$ V vs. NHE). In this work all potentials are given in NHE. A conversion to the pH-corrected hydrogen scale (RHE) was deliberately avoided, since in contrast to the competitive HER the CO formation on carbon based materials shows no or only low dependence on the pH value.⁶⁵ A Pt wire was located as a counter electrode (CE) in a separated electrolyte chamber. *Post mortem* XPS and electrochemical analysis showed no platinum or silver contamination of the WE under our experimental conditions (not shown). At the bottom of the cell, the WE (GDE) was installed with the catalytic layer towards the electrolyte, while the backside of the GDE was fed with the reactive gas in bypass mode.

The cell was filled with 5 ml of electrolyte C_i (0.5 M KHCO₃ and 0.5 M K₂SO₄, CO₂ saturated by CO₂ purging for 15 min, pH of the final conditioned electrolyte was measured to be 7.5 with a specific conductivity of 107 mS cm⁻¹) and the feed gas was drawn at the back of the GDE (CO₂,

CO, Ar) with a constant flow rate (250 ml h⁻¹). The membrane-based inlet system for the differentially pumped mass spectrometer (Pfeiffer, PrismaPlus) was located directly at the gas outlet of the cell. The response time for product detection was around 5 s relative to the current signal. The system was first purged with the feed gas for about 5 min to remove residual gases and to bring the GDE into equilibrium with the electrolyte, the LSV measurements were started with a scan rate of 5 mV s⁻¹, starting at -0.25 V (NHE). Here we would like to notice that, in contrast to the potentials given in most publications, we refrain from performing an iR-compensation for reasons of possible overcompensations that specifically might be observed at high current densities.

After each measurement calibration gases, composed of CO₂, CO, H₂ and CH₄ were passed at the backside of the GDE which allowed the conversion of the mass signals into concentrations (vol%) and thus the evaluation of the specific gas production rates (*SGPR*) and Faraday Efficiencies (*FE*). For these calibrations the GDE was still in contact with the electrolyte, however, no current was passing through the WE. Details on the data analysis can be found in the SI. It must be noted that the calculated *FE* given here refer to the gas composition at the outlet of the bypass underneath the cell. Since a certain proportion of the gaseous reaction products leave the cell through the electrolyte, these calculated *FE*_{gas} might underestimate the actual *FE* of the electrochemical reaction. As shown in more detail for a Pt/C-based reference measurement displayed in **Figure S1** in the SI this loss was determined to be about 10-15%.

For quantification of liquid products, the following respective potentials on NHE scale were applied to the GDE for 10 min and the electrolyte was subsequently analyzed by ion chromatography (IC): -0.5 V, -1.0 V, -1.4 V and -1,8 V (NHE) in cathodic sweep, and -1.5 V and -0.5 V (NHE) in further anodic return sweep. For that an “ECO IC” from Metrohm equipped with

a Metrosep Organic Acid's 250 / 7.8 column, was used. Degassed 0.5 mM H₂SO₄ was the eluent and IC standards from Sigma-Aldrich were used to calibrate the device.

2.4 *Post mortem* electrode analysis by XPS

For the *post mortem* XPS analyses, GDEs were drop-casted with a catalyst loading of 0.24 mg cm⁻² and used as a working electrode in CO₂-saturated 0.5 M KHCO₃ electrolyte instead of GDEs in the gas flow cell. Each measurement was performed on a freshly prepared electrode. The electrochemical protocol included the determination of the open circuit potential (OCP), followed by a LSV at 5 mV s⁻¹ to various potentials in the range of -0.5 V to -2.04 V either in the forward, or backward scan. These potentials were kept constant for 5 min. Subsequently, the electrodes were extracted from the electrolyte chamber at the respective potential, rinsed carefully with ultrapure water and dried under room temperature in a desiccator, before transferring them into the XPS system. The XPS analysis was performed on the GDE without the use of an additional (conducting) substrate. The amount of scans and kinetic energy were kept identical to the XPS measurements on the sole catalyst (cf. **Table S2** for details).

3. Results

3.1. Physico-chemical characterization of the catalysts

As shown and discussed in the SI on **Figure S2** and **Figure S3**, N₂-sorption measurements and Raman spectroscopy revealed similar surface area and carbon morphology for all samples. Both, N₂ sorption measurements and Raman spectra are dominated by the carbon support, while no particular influence of the different metal species can be deduced, as was expected.

XPS was used to get information about the surface near elemental composition and the chemical/oxidative states of the metal within the catalysts, as well as to identify possible impurities brought into the systems during preparation. **Figure S4** shows the survey scans for all investigated

M-N-C catalysts. The catalysts consisted merely of the elements N, C, O, Cl and the respective metal species. All catalysts were dominated by the presence of carbon as main element, as was expected since a carbon black was used as porous support material and only low porphyrin loadings were applied in the impregnation to avoid side phase formation. For the metal-free H₂-N-C catalyst as well as for KB600, the survey scans confirmed that no metal impurities could be found within the detection limits of XPS.

In **Table 1** the surface-near elemental concentrations of the metal [M], [N] and [C], are listed together with the N-to-M ratios. The entire elemental surface-near composition (including O and Cl concentrations), as well as the estimated atomic ratios in the precursor mixtures (calculated from porphyrin plus carbon support) can be found in **Table S3**. The measured ratios are approximately equal to the values that one would expect for the final M-N-C catalysts based on the composition of the initial precursor mixtures.

Table 1: Surface-near concentrations of M-, N- and C in the M-N-C catalysts (in at%) and the respective N-to-M-ratios.

Element	Mn-N-C	Fe-N-C	Co-N-C	Ni-N-C	Cu-N-C	Zn-N-C	Sn-N-C
M / at%	0.25	0.27	0.34	0.31	0.32	0.30	0.35
N / at%	1.04	1.11	1.36	1.25	1.33	1.23	1.40
C / at%	97.51	96.22	94.66	96.65	93.71	96.77	95.68
N-to-M /-	4.18	4.11	4.03	4.01	4.09	4.10	4.05

The metal content of all M-N-C catalysts was about 0.3 at%, which is close to the metal content of the initial precursor mixture of 0.4 at%. The nitrogen concentrations were approximately four times the metal concentrations as would be expected if only M-N₄ moieties were present as the

predominant M and N species. However, minor incorporations of oxygen and chlorine occurred in all catalysts, leading to a slight deviation from the values expected from the precursor compositions. As intended, small fractions of metal were leached out during the acid leaching. Overall, the measured concentrations were close to the composition in the precursors. This is due to the fact that at a pyrolysis temperature of 600 °C (as used in this work) a decomposition of the porphyrin may occur. Yet, the decomposition of the porphyrin core-structure, e.g. the M-N₄-center, is still widely suppressed as evidenced by thermogravimetric data from Bogdanoff et al. (2004).⁶⁶ A demetallation without impairment of the nitrogen species occurs only for a negligible fraction of the metal centers, leading to a N-to-M-ratio slightly larger than the initial value of four, as is in accordance with literature values.⁶⁷

Figure 2 shows the XP spectra of the N 1s region. The most pronounced feature was the presence of a double peak (398 eV and 400 eV) for the metal-free H₂-N-C, whereas only one peak, situated at binding energies between those two peaks, was observed for all M-N-C. Thus, the behavior is rather similar to what is found for the comparison of the free porphyrin base and metallo porphyrins.^{68,69} The peak position of the M-N₄ center depends on the central metal ion, the configuration of the M-N₄ center and the M-N bond length, yielding peak maxima at 398.2 to 398.7 eV.⁶⁸ This is due to the fact that such changes also affect the binding energies of the core electrons of the nitrogen.

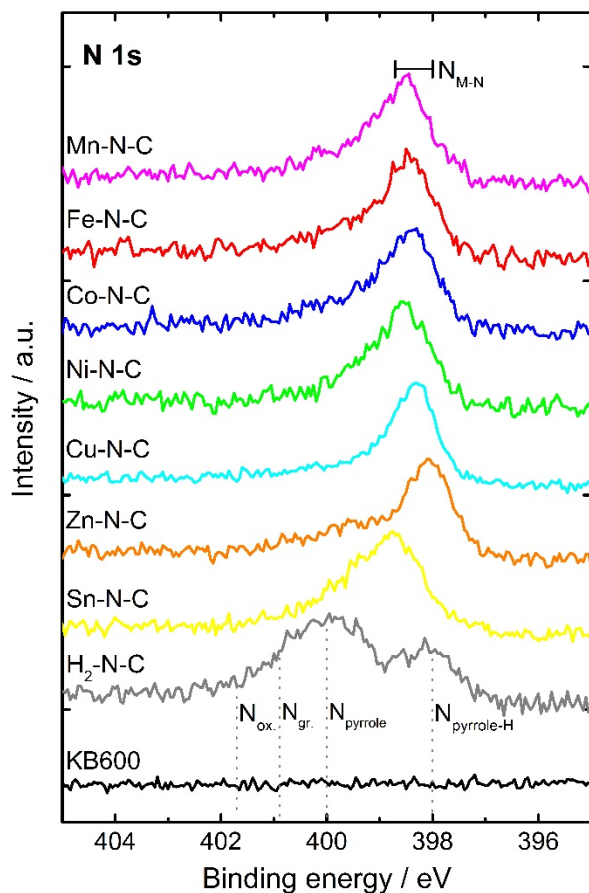


Figure 2. N 1s fine scan spectra of all catalysts normalized to their respective maximum peak intensity. The spectra of H₂-N-C and KB600 are displayed as references. Indicated are the approximate peak positions and position ranges, respectively, of the various nitrogen species: pyrrolic nitrogen without H (N_{pyrrole-H}), pyrrolic nitrogen with H (N_{pyrrole}), graphitic nitrogen (N_{gr.}), oxidic nitrogen (N_{ox.}) and metal bound nitrogen (N_{M-N}).

To emphasize the dependence of the N_{M-N} peak position on the respective metal center, the binding energies of the N_{M-N} peaks of our M-N-C catalysts are plotted as a function of the N_{M-N} binding energies in the related porphyrins as reported in literature in **Figure S5**.^{68,70,71} For most M-N-C catalysts, the position of the N_{M-N} peak is shifted to lower binding energies compared to the peak position found for metallo-porphyrins (but still at higher values compared to N_{pyrrole-H}).

As can be seen, the positions of the N_{M-N} peaks appear similarly affected by the electronic state of the metal in our M-N-C in comparison to the porphyrins. The similar behavior of our catalysts might indicate that most of the $M-N_4$ cores of the precursor actually remained intact in their pyrrolic structure after pyrolysis.

The measured N_{M-N} peaks in Figure 2 exhibit a slightly asymmetric shape. The reason for this asymmetry could not be clarified undisputably. We presume that the asymmetry might be caused by minor differences in the local environment of the supposed $M-N_4$ structures through low amounts of oxygen functionalization of carbon in the vicinity of the metal centers or through partial axial ligation of the metal center by (hydr-)oxygenation or chlorine ligation from the acid treatment. This might also explain the retained oxidation state of the catalysts with a chloroporphyrin precursor (Mn-, Fe- and Sn-N-C).

Overall, the predominant nitrogen species found in the M-N-C catalyst can be attributed by more than 90 % to N_{M-N} in a $M-N_4$ coordination. Species with even higher binding energies than $N_{pyrrole}$, that are typically reported as graphitic ($N_{gr.}$) and oxidic nitrogen ($N_{ox.}$), were solely observed for the H_2-N-C catalyst, yet in insignificant amounts.⁴⁹ The lower thermal stability of the H_2 -porphyrins in comparison to metalloporphyrins might be at the origin of this.^{72,73}

XPS fine scans of the metal regions are displayed in **Figure 3** and further confirm the presence of $M-N_4$ structures. All catalysts showed main peaks related to the oxidation states typically found in their respective porphyrins and expected for the resulting catalyst: M^{2+} for Co-,⁷⁴ Ni-,⁷⁰ Cu-,^{75,76} Zn-N-C;⁷⁷ M^{3+} for Mn-,⁷⁸ Fe-N-C;⁷⁹ M^{4+} for the Sn-N-C.^{56,80} Please note that the quality of the metal-spectra, e.g. the signal-to-noise-ratio, strongly depends on the respective relative sensitivity factor (R.S.F.) of the metal, which is lowest for Mn and Fe and highest for Cu and Zn. The Co- and Cu-N-C catalysts (Figures 3c and e) showed minor features of a metallic M^0 state at binding

energies slightly lower than their main peaks ($< 1\%$ of the overall metal content). For Mn-, Fe-, Co- and Cu-N-C, satellite features of the respective oxidation states were observable. For Co-N-C, a slight shoulder can be observed at ~ 781.8 eV next to the main peak at 780.5 eV, that can most likely also be assigned to $\text{Co}^{2+}\text{-N}_4$, yet in a slightly different configuration.⁸¹ This observation was further made for a pristine CoTMPP immobilized on an amorphous fumed silica.⁶⁷ In this case, however, we refrain from a definite assignment of this peak. Nevertheless, close to 100 % of the total metal contents can be attributed to a M-N₄ coordination.

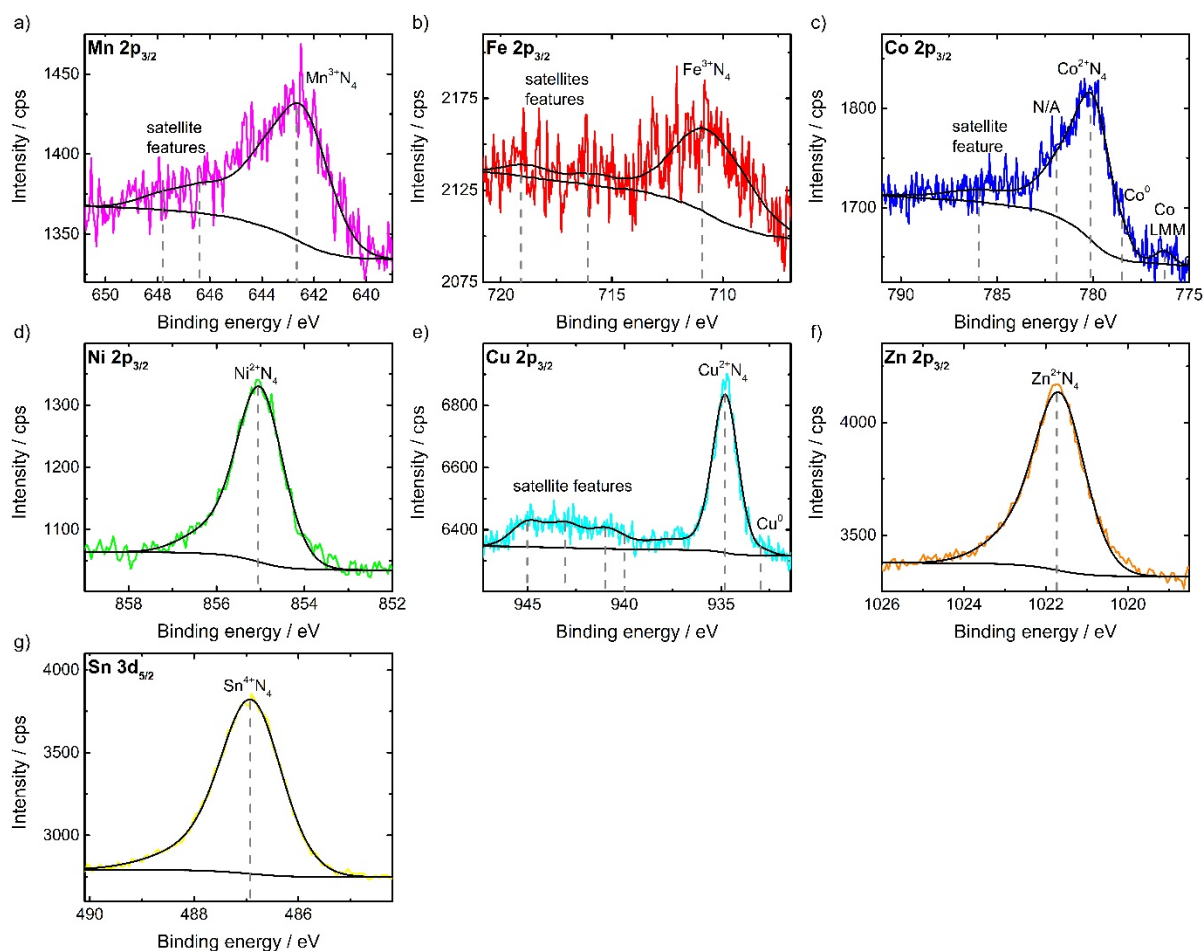


Figure 3. XPS fine scan spectra of the metal species in M-N-C catalysts: Mn 2p_{3/2} (a), Fe 2p_{3/2} (b), Co 2p_{3/2} (c), Ni 2p_{3/2} (d), Cu 2p_{3/2} (e), Zn 2p_{3/2} (f), Sn 3d_{5/2} (g). Indicated are the peak positions where the presumed metal species can be found.

The respective O 1s and Cl 2p fine scan spectra of the catalysts are displayed in **Figure S6**. For a more detailed interpretation of the O 1s, Cl 2p and C 1s spectra the interested reader is referred to the brief discussion in the SI. In summary, the following conclusions can be made: Oxygen is mainly present in the catalysts in the form of carboxyl and carbonyl groups and minor fractions of hydroxides. The only chlorine species that were identified to significant amounts were C-Cl bonds originating from the acid leaching in HCL. Carbon within the catalysts is mainly consisting of sp²-hybridized carbon and oxygen-functionalities, as indicated in the spectra found in **Figure S7**.

If the overall set on XPS data is considered, it can be concluded, that the M-N₄-structure of the porphyrin cores are mainly left intact and integrated into the pyrolyzed catalyst material, which is a rather unique feature considering the materials discussed in literature.

3.2. Electrochemical characterization of the M-N-C catalysts

The electrochemical characterization and related product identification was performed for all samples via LSV in GDE configuration as described in the experimental section and the SI.

Figure 4 shows that the various M-N-C samples reveal very individual current-voltage behaviors under CO₂ feed to the GDE. As a first very rough result, the obtained current densities vary widely between Fe-N-C as the most active catalyst and Mn-N-C as the least active material. In between, the other M-N-C samples, as well as H₂-N-C and KB600, roughly line up in the order of decreasing activity as follows: Fe > Ni > Co > KB600 > Cu > H₂, Sn, Zn > Mn.

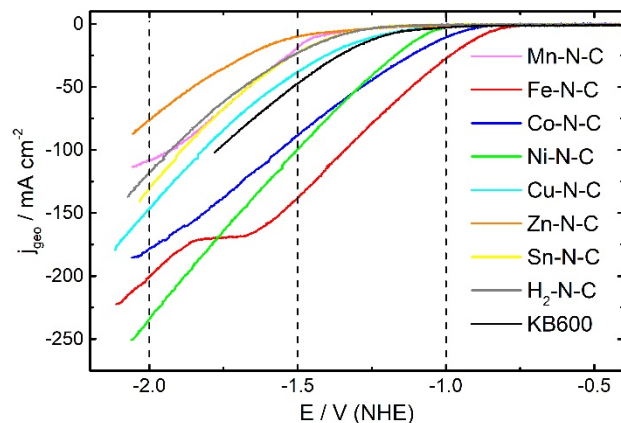


Figure 4. LSV of the different catalysts measured in 0.5 M C_i electrolyte with CO_2 feed to the GDE at a scan rate of 5 mV s^{-1} . The dashed lines indicate the potentials for which $SGPR$ and FE were extracted for later discussions.

In order to assess to what extent the current densities are actually based on a reduction of CO_2 , the product composition of the cell's gas outlet was simultaneously measured to the corresponding current density responses in Figure 4. From these measurements the standard gas production rate ($SGPR$) and Faradaic efficiency related to gas products (FE_{gas}) were calculated (procedure is described in the SI).

At this point we would like to remind that the FE_{gas} values are a lower estimates of the actual FE for the gases produced during the electrochemical reaction as parts of them will leave the system through the electrolyte. A more detailed discussion on this is found in the SI for a Pt/C-based reference measurement as displayed in Figure S1.

Each of the M-N-C catalysts were investigated using three different feed gases: CO_2 , Ar and CO within a potential range from -0.4 to -2.2 V (NHE). The measurements under CO-feed were carried out in order to investigate to what extent CO could act as an intermediate product in the formation of hydrocarbons. Measurements with Ar-feed instead of CO_2 serve as a reference in order to show

the impact of gaseous CO₂ at the GDE on the electrochemical activity and to estimate to what extent CO₂ might suppress the formation of hydrogen gas. However, we have to note that a direct comparison of Ar- and CO₂-measurements is only reasonable at low current densities, since under Ar the pH in front of the GDE is continuously shifted to higher values with increasing current density compared to the measurements under CO₂ feed. Thus, a comparison of the current and *SGPR* curves is still possible close to the onset potential, whereas at higher current densities the curves drift to significant more negative potentials compared to the CO₂ based measurements. A more detailed explanation of this effect is given in the SI.

The data for blank KB600 without any pyrolysed porphyrine are shown as a reference measurement in **Figure S8**. The complete datasets obtained on current-voltage curves and *SGPR* as well as the corresponding FE_{gas} for the porphyrine-based samples are displayed in **Figure S9** to **Figure S16**, with ascending figure number in the order of Mn-, Fe-, Co-, Ni-, Cu-, Zn-, Sn-, H₂-N-C. Even though the data contain a wealth of information about the behavior of the various catalysts, in the following we will focus our discussion only on the main trends and results which can be deduced from these measurements.

Using Ar-feed beside H₂ only negligible amounts of CO (*SGPR* approx. 1-2 $\mu\text{mol h}^{-1} \text{cm}^{-2}$) were detected for all samples. As those *SGPR* values were lower by a factor of about 1000 in comparison to measurements under direct CO₂-feed, they were not considered in the further discussion. Obviously the supplied CO₂ is the main source for the CO₂RR at the GDE and not any carbonate from the electrolyte.

Using CO₂-feed Figures S9 to S16 reveal that, in contrast to the metal-containing samples, the metal-free sample H₂-N-C and also the carbon support KB600 show only hydrogen production but no reduction of CO₂ to gaseous products and no soluble products were found in IC measurements.

Obviously, the presence of a metal is necessary for the CO₂RR in our samples and varies with the selected metal.

The product-specific activities of the M-N-C catalysts towards CO₂RR are summarized in **Figure 5** for the three potentials -1.0, -1.5 and -2.0 V (NHE). It should be noted, that beside the listed products no other gaseous products could be detected within our measuring sensitivity (approx. 1 μmol h⁻¹ cm⁻²).

Various groupings among the catalysts with regard to the CO₂RR activities are observable: Fe-, Co- and Ni-N-C show by far the highest activity for the CO₂RR at all potentials and form CO at high *FE* (*FE* ≈ 50 - 90 %, *SGPR* ≈ 1 - 4 mmol h⁻¹ cm⁻²). As will be described in more detail below, the HER is only partially suppressed for Co-N-C over the whole applied potential range. For Fe-N-C the HER is almost completely suppressed down to a potential of -1.5 V (NHE) and for Ni-N-C over the entire investigated potential range. In comparison to this, Cu-, Zn-, and Sn-N-C catalysts reveal, in strong competition with the HER, only moderate CO₂RR activities and produce little amounts of CO (*FE* < 25 %, *SGPR* < 0.5 mmol h⁻¹ cm⁻²), while Mn-N-C shows only traces of CO (*SGPR* ≈ 0.015 mmol h⁻¹ cm⁻²).

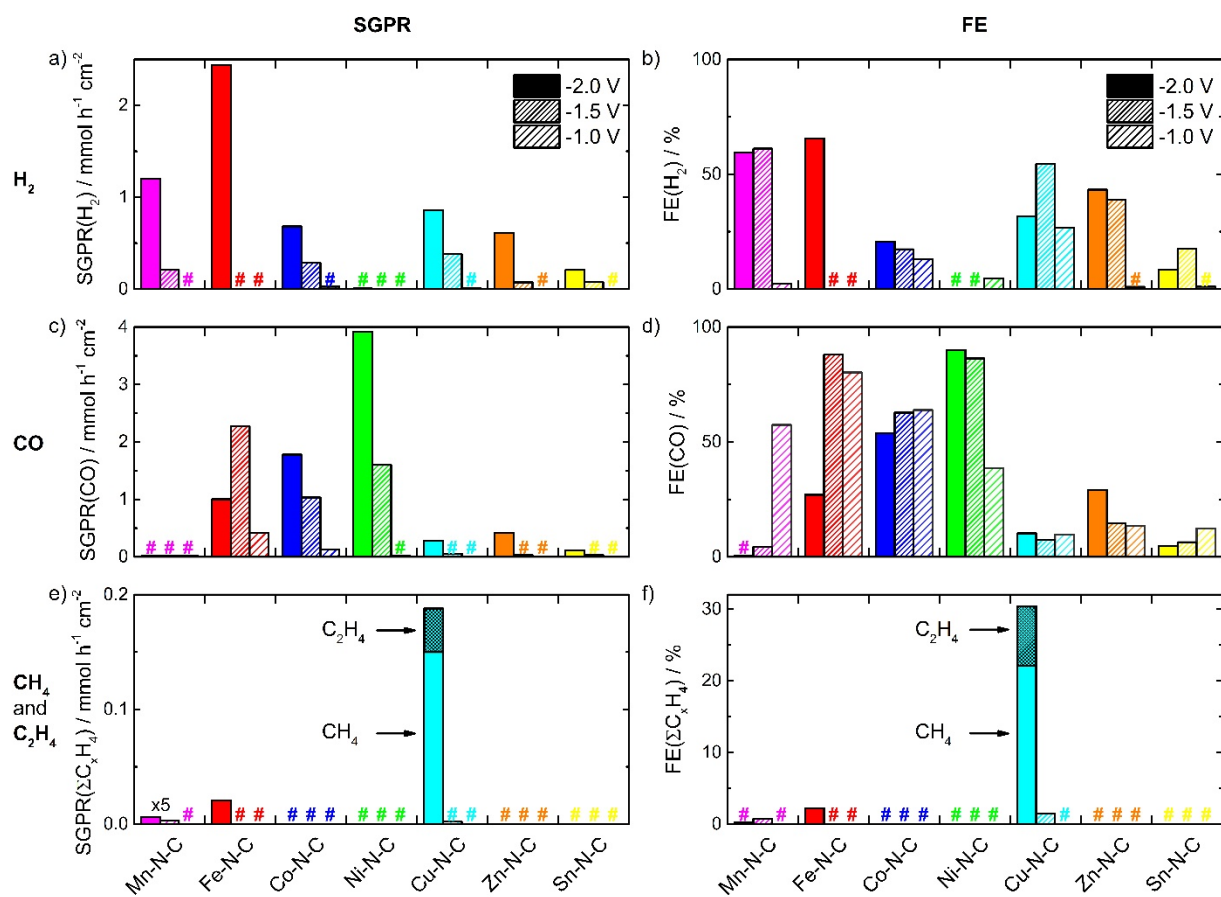


Figure 5. *SGPR* and *FE* of H₂ (a and b), CO (c and d) and CH₄ and C₂H₄ (e and f) displayed for each catalyst at -2.0 V (left), -1.5 (middle), -1.0 V (right) vs. NHE. “#” indicate that the values for the measured data points are too low to properly be displayed.

The Cu-N-C, and on a significantly smaller scale Fe- and Mn-N-C, were the only catalysts able to produce CH₄, each at potentials more negative than -1.5 V (NHE) and always in the presence of a simultaneous HER. Furthermore, Cu-N-C is further capable of forming C₂H₄ in significant quantities (*SGPR* at -2.0 V (NHE) \approx 40 μ mol h⁻¹ cm⁻², *FE* \approx 8 %). The onset potentials for all gaseous reaction products are summarized in **Table S4** for the overall group of catalysts.

In **Figure 6** the total of gaseous faradaic efficiencies (*FE_{gas}(total)*) are displayed as the sum of the respective *FE_{gas}* for H₂, CO, CH₄ and C₂H₄ for all M-N-C. Especially Sn-, but also Zn-, Cu- and

Mn-N-C tend to show lower $FE_{\text{gas}}(\text{total})$ values than the other catalysts. As can be seen in **Figure S17**, IC-analysis of the electrolyte after potentiostatic electrolysis over 10 min at the given potentials reveals formate production rates for these catalysts in the following order: Sn \gg Cu $>$ Zn $>$ Mn in M-N-C. No soluble products that could have been detected via IC (formate, acetate etc.) could be observed for the other catalysts. On Sn-N-C, formate formation of about $0.2 \text{ mmol h}^{-1} \text{ cm}^{-2}$ at -1.8 V (NHE) accounts for a FE of about 30 - 40 %, which explains the rather low $FE_{\text{gas}}(\text{total})$ for gaseous products. For Zn-, Cu- and Mn-N-C correspondingly less formate production rates ($< 0.05 \text{ mmol h}^{-1} \text{ cm}^{-2}$) and $FE < 15 \%$, were measured. No other products could be detected in significant amounts via IC and headspace GC, but can of course not be completely ruled out.

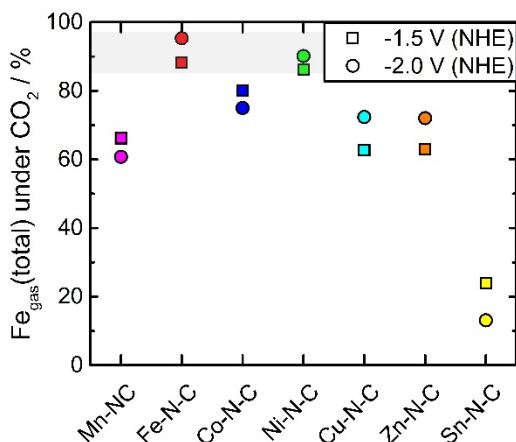


Figure 6. $FE_{\text{gas}}(\text{total})$ for all M-N-C at -1.5 V and -2.0 V (NHE) , determined from the sum of the individual FE_{gas} for H_2 , CO , CH_4 and C_2H_4 . Due to the limited collection efficiency of products at the GDE, a FE_{gas} measured here of around 85-90 % corresponds to a real FE at the electrode of around 100 %, as indicated by the area marked in grey.

The observed strong competition between HER and CO₂RR on the most active catalysts Co-N-C, Fe-N-C and Ni-N-C is illustrated in detail in the potential-dependent *SGPR* curves in **Figure 7**.

For Co-N-C, the onset potentials for both H₂ and CO formation are very similar (-0.76 and -0.79 V (NHE), cf. Table S4), accompanied by a steady increase in both production rates with increasing overpotential (Figure 7a). However, the CO₂RR is significantly preferred over the HER in the entire potential range ($FE(\text{CO}) \approx 60\%$, $FE(\text{H}_2) \approx 15\%$ at 90 mA cm⁻² for -1.5 V (NHE)).

Switching from CO₂ to Ar, the H₂ formation as sole product starts at an onset potential of -0.81 V (NHE), which is almost unchanged to the CO₂-based measurement, considering the small positive pH shift due to the Ar-feed (see SI). The *SGPR*(H₂), however, is more than doubled with a $FE(\text{H}_2)$ of roughly 70 %, compared to the CO₂-feed measurement. We conclude that the CO₂RR and the HER compete to high extent for the same reaction sites on the Co-N-C catalyst.

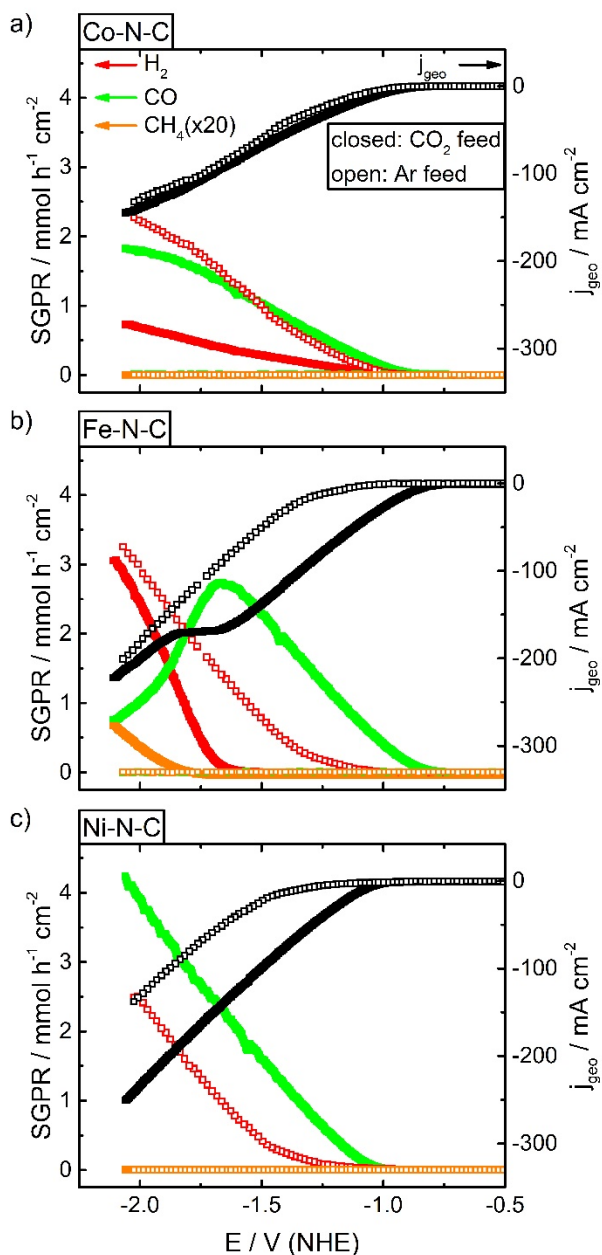


Figure 7. SGPR of H_2 (red), CO (green) and CH_4 (orange), as well as j_{geo} (black) measured in CO_2 (filled squares) and Ar (open squares) of Co-N-C (a), Fe-N-C (b) and Ni-N-C (c).

High FE_{gas} towards CO formation have also been confirmed by Zhang et al. (2018) based on DFT calculations and experimental studies of non-pyrolyzed Co-Phthalocyanine.⁸² They found, that the activity for the reaction of CO_2 to CO results from moderate binding energies of $^*\text{COOH}$

and *CO on the Co-N₄ active site and thus an optimal *CO desorption. A similar effect might apply for our Co-N-C catalyst. For other metal-phthalocyanines (Fe-, Ni-, Cu- and Mn-Pc) however, Zhang et al. could not observe a significant CO formation, whereas we observed on our Ni-N-C and Fe-N-C catalysts the highest activities and *FE*(CO) of all investigated catalysts. On the one hand, this could indicate that the incorporation of the M-N₄ centers into the graphene network could improve their catalytic activity for the CO₂RR compared to the molecular centers in isolated organometallic materials, as observations previously made for Fe- and Co-N-C catalysts for the ORR indicated.^{66,67,83,84} On the other hand is the nature of the local M environment during the reaction not yet investigated thoroughly enough and might therefore also slightly differ from M-N₄.

The Fe-N-C shows the most positive onset potential for the CO production among all investigated catalysts (-0.71 V (NHE), cf. Table S4). In contrast to the Co-N-C the H₂ evolution is almost completely suppressed up to a potential of around -1.4 V (NHE). This suppression is particularly evident from the comparison with the Ar-measurement, where the HER as the sole reaction already starts at about -0.9 V (NHE) (-0.82 V when taking the pH-shift due to Ar-purging into account, cf. SI) and increases rapidly with increasing overpotentials (Figure 7b). Due to the HER suppression, the Fe-N-C is the most effective catalyst for CO formation in this potential range, with a *FE*(CO) of approx. 80% and a current density of 150 mA cm⁻² at -1.5 V (NHE). Sweeping towards potentials lower than -1.4 V (NHE), the HER is no longer suppressed and increases rapidly to the detriment of CO formation rates. It should be pointed out that at such high current densities the pH value in front of the GDE is strongly shifted to higher pH values due to the proton consumption by HER and CO formation. This has already been demonstrated by Burdyny and Smith (2019).⁸⁵ However, such a pH shift does not seem to be the reason for the

sudden change from CO formation to HER (*e.g.* by pH-dependent depletion of CO₂), as a similar current density plateau can not be observed for Ni-N-C under similar current densities and experimental conditions.

A further special feature of Fe-N-C is that at approx. -1.7 V (NHE) (0.3 V more negative than the HER onset potential) a significant formation of CH₄ is observable (Figure 7b). Apparently, intermediates of the HER are required for the hydrogenation of CO₂. However, this is not observed on the Co-N-C catalyst, despite the presence of HER and CO. The capability of hydrogenation of CO₂ must be due to specific catalytic properties of Cu- and Fe-N-C. Either the interaction of molecular M-N₄ units with other catalytic sites or a change in the electronic state related to M-N₄ centers could be at the origin, *e.g.* through reduction of M²⁺ ions to M¹⁺ or M⁰. Evidence of such a mechanism can be found in literature and is discussed below.⁵²

In the case of Ni-N-C, when measured with Ar-feed, the HER starts at -0.79 V (NHE) (ca. -0.71 V considering the pH shift due to Ar-purging). In contrast, under CO₂-feed, the HER is completely suppressed over the entire investigated potential range, with CO as only significant gaseous product (Figure 7c and **Figure S12**), starting at an onset potential of -1.0 V (NHE). The CO formation continuously increases to a potential of -2.2 V (NHE) where a *SGPR* of 4 mmol h⁻¹ cm⁻² with a *FE*_{gas} > 90 % at a current density of -250 mA cm⁻² is reached. This is an excellent performance that is similar to an Ag-loaded GDE that was also measured in 0.5 M Ci buffer.⁸⁶ For a Ni-N-C catalyst prepared by a pyrolysis of a polyaniline/Ni-salt mixture, Möller et al. (2019) showed the applicability of this type of M-N-C catalyst in a real electrolyzer configuration, demonstrating high performance towards CO formation and similar *FE* and current densities as we showed for our Ni-N-C catalyst.⁸⁷

In summary, the HER onset potentials of the discussed catalysts are shifted to more negative potentials in the order $\text{Co} > \text{Fe} \gg \text{Ni}$ in M-N-C due to the presence of CO_2 . Apparently, H_2 and CO formation compete for the same catalytic center, where the CO_2RR is preferred over the HER. This competitive mechanism allows for high $FE(\text{CO})$.

In order to better understand the different influences of the various M-N₄ centers on the HER suppression by CO_2 , more in-depth studies on the electronic structure of the centers during the reaction conditions are required. *Operando* XPS could provide information on changes occurring on the catalysts surface as induced by electrochemical reactions. Unfortunately, with the low metal ion concentrations in our samples (< 1%) synchrotron radiation would be necessary in order to obtain good spectra in a reasonable time, which was not within the scope of this work.

The gas specific current densities calculated for Fe-, Co-, Ni- and Cu-N-C are displayed in **Figure S18**. Even though the overall current density and production rates are not among the most active samples, the Cu-N-C is very interesting from a scientific point of view because it has by far the highest formation rate for CH_4 (up to $0.16 \text{ mmol h}^{-1} \text{ cm}^{-2}$ at -2.0 V (NHE)) among the investigated catalysts and is the only catalyst that produces C_2H_4 , as is shown in Figure 5.

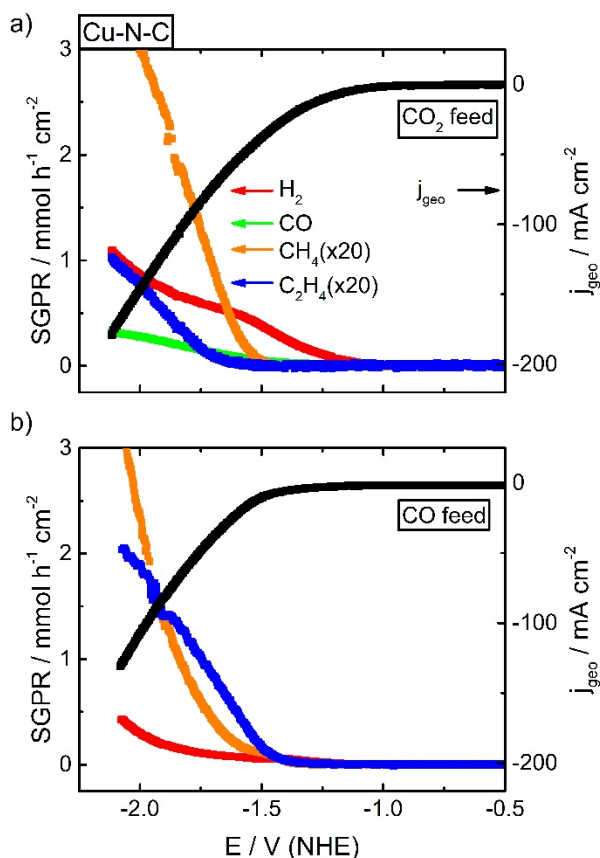


Figure 8. SGPR of H₂ (red), CO (green), CH₄ (orange) and C₂H₄ (blue), as well as j_{geo} (black) of Cu-N-C measured in CO₂ (a) and CO (b).

In **Figure 8** the SGPR and the corresponding voltammograms of Cu-N-C with CO₂ feed (Figure 8a) and CO feed (Figure 8b) are re-plotted from **Figure S13**. Under CO₂-feed, on Cu-N-C the H₂ formation seems not or only to a small extent being suppressed (cf. Figure S13a and c), starting at a potential of about -0.9 V (NHE) (cf. Table S4) and accompanied by a minor production of CO with a $FE(\text{CO})$ of approximately 10 %. The onset potential for the CH₄ formation lies at -1.5 V (NHE) and at -1.75 V (NHE) the formation of C₂H₄ is initiated. With the onset of the hydrocarbon production in return, the slope of the HER rate decreases slightly, as hydrogen is consumed to form hydrogenated products. This reduces the $FE(\text{H}_2)$ to about 30 % at -2.0 V (NHE)

in favor of the $FE(\text{CH}_4)$ and $FE(\text{C}_2\text{H}_4)$ of approx. 20 % and 10 %, respectively. This clearly shows that the formation of CH_4 and C_2H_4 is somehow coupled to reactive intermediates of the HER.

When CO is fed to the electrode, as shown in Figure 8b, on the one hand the CH_4 formation starts at about the same potential as under CO_2 , but with a slightly lower $SGPR$, while on the other hand the $SGPR(\text{C}_2\text{H}_4)$ is increased significantly. What is remarkable, is a shift of the onset potential for the C_2H_4 formation under CO-feed by 0.2 V towards more positive potentials, with an increase of the $FE(\text{C}_2\text{H}_4)$ by a factor of 2 to 2.5 (**Figure S19**). Apparently, CO is an intermediate for hydrocarbon formation and specifically for the formation of polynuclear hydrocarbons high CO concentrations are required. Similar observations have also been made by other groups investigating CO as feed gas.^{88–90} The CO coverage seems to be a limiting factor of hydrocarbon formation what is in accordance with the adsorption energies provided by Nitopi et al. for metallic Cu catalysts.⁹¹ Measurements under CO feed were also carried out with all other catalysts (cf. Figure S9 to Figure S16). However, the $SGPR(\text{CH}_4)$ on Cu-N-C is by a factor of 100 larger in comparison to Fe-N-C and Mn-N-C.

Obviously, there is a certain similarity in the CO_2RR reactivity of some M-N-C catalysts with that of metallic catalysts as investigated by Hori and co-workers.¹⁴ In this context the question arises whether the Cu-N-C catalysts undergo structural and electronic changes, *e.g.* a reversible reduction to metallic structures, which would enable the formation of hydrocarbons. Similar effects have already been observed for copper(II) phthalocyanine (CuPc) by Weng et al. (2018)⁶² and for a non-purified Cu-N-C catalyst pyrolyzed at high temperatures by Karapinar et al. (2019)⁶³ In an approach to investigate the state of copper at different reaction conditions in our Cu-N-C catalyst *post mortem* XPS analysis was performed at various stages of electrolysis.

3.3. Potential-dependent *post mortem* XPS analysis of Cu-N-C/GDE

The GDE were extracted from the electrochemical cell for the *post mortem* XPS analysis at various conditions (1) to (6), which are indicated in **Figure 9**. While for conditions (1) – (5) a single LSV with subsequent chronoamperometric hold (20 min) at the related potential was performed, for condition (6) the catalyst was first swept to -1.9 V (NHE) and then cycled back to -0.4 V (NHE). For conditions (1) and (6) unambiguously no electrochemical reactions are occurring, while condition (2) is close to the onset of H₂ and CO formation as measured in the MS-coupled bypass experiments. The absolute current densities measured in the *post mortem* experiments are slightly lower than in the MS-coupled LSV measurements, but the onset potential and the trend of the curve are comparable.

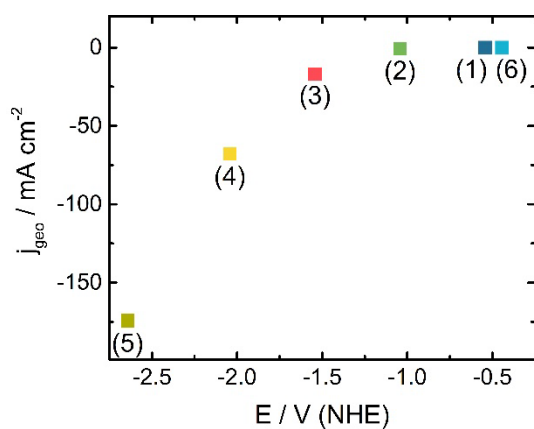


Figure 9. Observed current densities from the LSV experiments performed in CO₂ saturated electrolyte for the *post mortem* XPS measurements of Cu-N-C. The points indicate at which potential the electrodes were taken out of the cell for further analysis.

Figure 10a and **b** show the according Cu 2p_{3/2} and N 1s fine scan spectra, of the initial catalyst powder, the catalyst ink impregnated on a GDE, the electrode after 5 min in the CO₂ saturated electrolyte at OCP condition (+0.30 V (NHE)), as well as at conditions (1) – (6). Furthermore,

based on these spectra, Figures 10c and 10d reveal the potential-dependent relative structural changes at the catalysts surface for Cu- and N-species.

Already from Figures 10a and b structural changes of the Cu 2p and N 1s signatures are visible. As Figure 10c shows, the initial Cu^{2+} state (representative for Cu-N₄) remains unchanged down to a potential of -0.5 V (NHE), with a relative contribution of more than 98 %. A further decrease in potential to -1.5 V (NHE) leads to a decrease in Cu^{2+} species to about 78 %, while at the same time a Cu^0 species occurs, that increases from less than 2 % up to 22 %. Up to -2.6 V (NHE) the relative concentration of Cu^0 only slightly increased further to 27 %. The reduction of the oxidation state from Cu^{2+} to Cu^0 seems at least partially reversible, since with sweeping the potential back to -0.4 V (NHE) the contribution of Cu^{2+} turns back to about 90 % and an according decrease in Cu^0 is observable. To what extent this reversible change of the oxidation state is connected to a reversible change in the environment will be addressed below. The main change in structure and oxidation state occurs in the potential range where the formation of CH_4 and C_2H_4 occurs in the MS-coupled LSV experiments.

Interestingly, at a similar potential of approx. -1.4 V (NHE) Hori et al. (1989) and Baturina et al. (2014) observed the formation of CH_4 and C_2H_4 on their metallic copper electrodes and on carbon-supported Cu nanoparticles, respectively.^{14,92} Thus, it is likely that for the Cu-N-C catalyst the formation of metallic species is responsible for the formation of hydrocarbons. The formation of metallic phases or clusters also makes the formation of polynuclear hydrocarbons (C_2H_4) more understandable, since its formation would have appeared unlikely on spatially separated Cu-N₄ centers.

Along with the changes in Cu 2p_{3/2}, a clear potential-dependent change in the N 1s signature of the Cu-N-C catalyst was visible (Figure 10d). Induced by the ink based electrode preparation the

main peak in N 1s of *Electrode_{as-prep}* was shifted to slightly higher binding energies compared to the plain catalyst powder, indicating a slight depletion in electron density at the metal center.⁹³ Furthermore, was a minor increase in relative pyrrolic N concentrations for the drop-casted catalyst layer compared to the pristine material observed. When brought into contact with the electrolyte at an OCP of about +0.3 V (NHE) a partial demetallation at the Cu-N₄ center seems to occur, as the relative concentration of N_{M-N} decreases from 92 % to about 84 %, while the concentration of pyrrolic N increases from 8 to 16 %. As soon as the potentials were applied, the underlying peaks became more intense, while at the same time the peak at 398.5 eV corresponding to N_{M-N} decreased in intensity. Moreover, this process appeared to be irreversible within the potential range applied, as for condition (6) the spectra is very similar to (5) at -2.6 V (NHE) but differs significantly compared to (1) at -0.5 V (NHE).

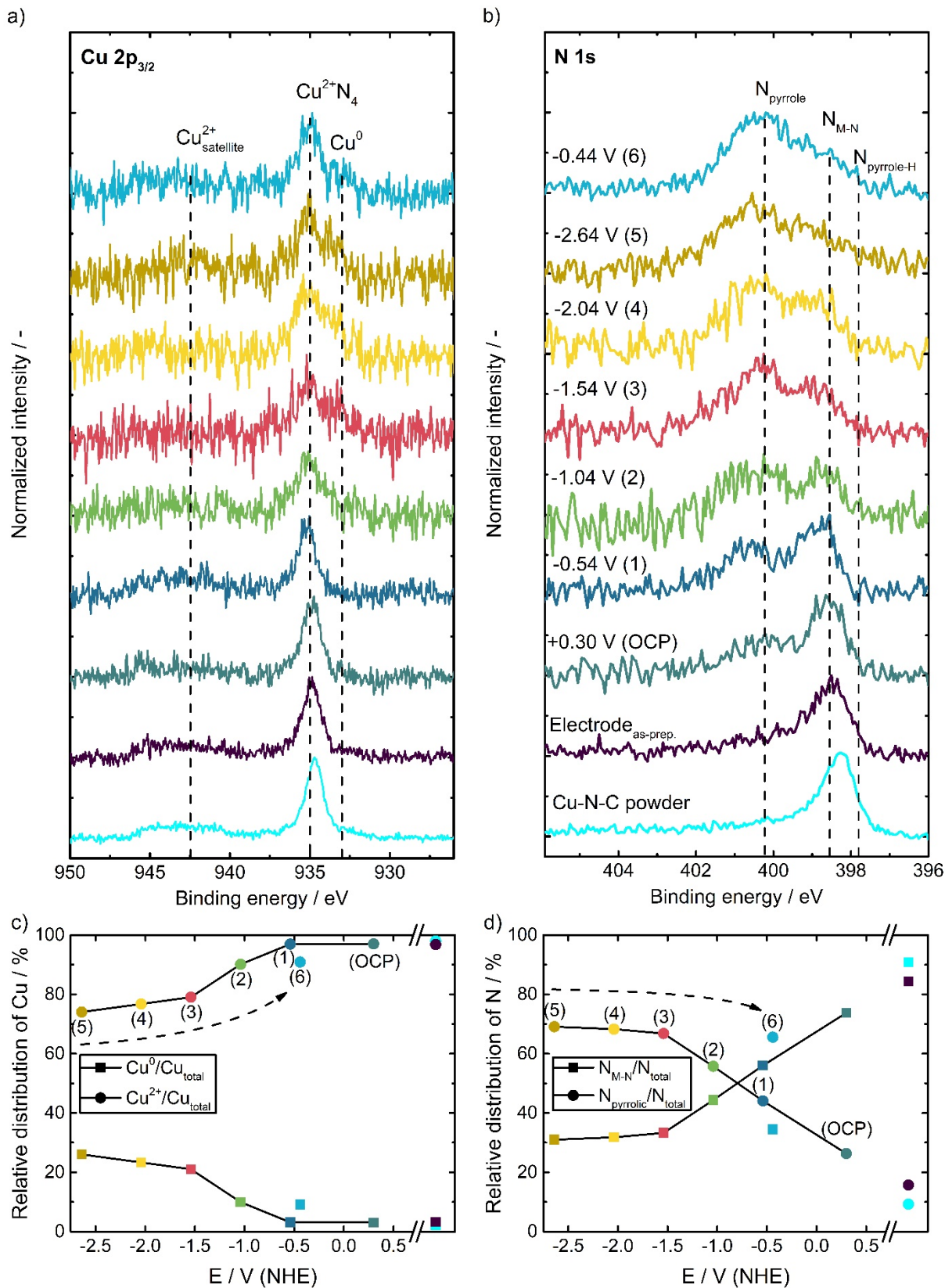


Figure 10. *Post mortem* XPS of the Cu-N-C catalyst. Shown are the Cu 2p_{3/2} (a) and N 1s (b) spectra obtained after different electrochemical potentiostatic conditions (OCP and conditions (1) to (6)), as well as the as prepared electrode (*Electrode_{as-prep.}*, purple) and the initial Cu-N-C catalyst powder (cyan). Further shown are the respective relative distribution of Cu- (c) and N-species (d) as functions of applied potentials. N_{pyrrolic} represents the sum of N_{pyrrole} and N_{pyrrole-H} concentrations.

Considering that a partial re-oxidation of the formed metallic species occurred without a significant reformation of metal-bound N, it is likely that to some extent Cu-N₄ centers are irreversibly disintegrated and that the formed oxidized Cu-species are no longer coordinated by nitrogen atoms.

Nevertheless, Cu²⁺ seems to remain in the catalyst material. In contrast to Weng et al. (2018)⁶² and Karapinar et al. (2019)⁶³, we cannot validate their conclusion on a reversible change upon electrochemical conditioning. As the reversibility is reported for both, a molecular and a pyrolyzed Cu-based catalyst, it is likely that the differences in observations might be due to slight differences in the experimental conditions, as they investigated the reversibility for a lower applied potential window. The clustering of Cu particles is likely to increase both with increasing overpotential and electrolysis time, making a re-oxidation and reformation of the Cu-N₄ center less likely.

In the context of these results, we can better understand the observations that were made during a first stability measurement on the Cu-N-C catalyst, as shown in **Figure S20**. In a potentiostatic experiment at -1.95 V (NHE) over 18 min under CO₂ feed, a steady increase in C₂H₄ and H₂ production can be seen over time, while the CH₄ formation continuously decreases. It is conceivable that as the electrolysis time progresses, Cu-N₄ centers are continuously reduced to

metallic clusters or phases and accumulating to larger extent over time, so that the C₂H₄ formation is preferred over CH₄ formation with ongoing electrolysis time.

4. Discussion and Conclusions

Numerous publications investigate the CO₂RR activities and selectivities of M-N_x centers, but often only for a specific type of metal ion in the center.^{30,49} As one of the few overarching studies, Ju et al. (2017) pursued a similar approach to our work using a set of uniformly prepared M-N-C catalysts.⁹⁴ In contrast to our samples, however, they found significant quantities of pyridinic, pyrrolic and graphitic nitrogen as well as small amounts of metallic species as by-products in their catalysts, what makes it more difficult to assign the CO₂RR activity to a particular active site. The authors introduce a DFT-simulated model for M-N₄-C centers with which they can successfully correlate the binding energy of the intermediates COOH * and CO * as descriptors for the onset potential and the reaction rate of the CO formation at moderate overpotentials in their measurements.

Overall, our measurements confirm this concept as the onset potentials (cf. Table S4) show an analogous trend (Fe < Co < Mn << Ni, Cu) and, with the exception of Mn-N-C, also the *SGPRs*(CO) follow their model (Fe > Co > Ni, Cu) (cf. Figure 5c). Although the Mn-N-C shows the predicted high *FE*(CO) of over 50 % (Figure 5d), the observed a *SGPR*(CO) was too low in comparison to the theoretical model.⁹⁴ This indicates that besides the catalytic centers also other factors play a decisive role. Especially for Mn-N-C, Zhang et al. (2019) showed that the activity could have been influenced by axial coordinated halide ions.⁴⁸ Furthermore, the carbon environment can have a decisive influence.⁹⁵

Since both, our catalysts and those of Ju et al. fulfill their model calculated for M-N₄-C centers, it can be assumed that at low overpotentials M-N₄ centers are primarily responsible for the CO₂RR

in both cases.⁹⁴ The generally increased competitive HER activity observed for the M-N-C catalysts of Ju et al. in comparison to our catalysts could possibly be explained by the reported side phases found in their catalysts. While we observe an almost complete suppression of the HER with Ni-N₄-C up to -2.2 V (NHE) and over a wide potential range also with Fe-N₄-C, Ju et al. give potential-dependent $FE(H_2)$ values of well over 20 %. For Co-N-C they even indicate a potential-independent $FE(H_2)$ of approx. 90%, whereas we only measure 20 % but a high selectivity of 50 – 60 % for the CO formation (cf. **Figure S11b**). These results show that with catalysts that exclusively contain M-N₄ centers a high selectivity towards the CO production can be achieved. To what extent these differences could be due to the use of a GDE configuration in our experiments as compared to Ju et al. is unknown. In principle, however, high CO₂ concentrations will certainly favor the CO₂RR compared to the HER.

According to literature, the prerequisite for CH₄ formation is a high binding energy of CO* and a low affinity for HER at the M-N₄ center.^{25,47} Based on the DFT calculations by Rossmeisl's group, this is the case for Co-, Fe- and Mn-N₄-C centers, but not for Cu-N₄-C.⁹⁴ In fact our Fe-N-C and Mn-N-C catalysts show the formation of small amounts of CH₄ with $FE(CH_4) < 5$ %. In contradiction to these calculations, however, no CH₄ is observed on Co-N-C, whereas on Cu-N-C CH₄ and even C₂H₄ as the main products of CO₂RR were observed with a summed $FE(C_xH_4)$ of approx. 30%. Indeed, our post mortem XPS results on Cu-N-C give strong hints that the activity towards hydrocarbons is mainly connected to the formed metallic structures formed at negative potentials instead of the Cu-N₄ center. Similarly, Varela et al. (2019) hypothesized that the overall CO₂RR activity of their Cu-N-C catalyst was based on finely dispersed metallic Cu particles on the carbon support, while Cu-N₄ sites play a subordinated role in the reaction.⁴⁹

From these results the general question arises to what extent the M-N_x center in M-N-C catalysts retain their integrity under operational conditions. Concerning Fe-N-C catalysts, *operando* EXAFS measurements by Leonard et al. (2018) indicate a partial reduction of the Fe²⁺ ion to Fe¹⁺ and Fe⁰ in the catalytic center at potentials of negative approx. -1.5 V (NHE).⁵² In fact, we see significant changes in the catalytic properties on our Fe-N-C in this potential range, as the CO₂RR to CO suddenly switches to the HER accompanied by a CH₄ formation. For Zn-N-C catalysts, however, Yang et al. (2018) reported that the Zn-N₄ center has a remarkable stability at least at -0.82 V (NHE) and is responsible for the high *FE* of up to 90 % at -4.8 mA cm⁻² for CO formation.⁹⁶ In comparison, our Zn-N-C only achieves about 15 % *FE*(CO) at a comparable potential and increases to about 30 % at -2.2 V (NHE). This again might be caused by multiphase contributions in their catalyst in comparison to the higher purity of Zn-N-C in our work.

Structural changes in dependence of electrolysis time may also explain some differences in the observed formation rates and *FE* measured by our instantaneous product detection method in comparison to the analysis of products accumulated over a longer period of time. This further demonstrates the difficulty to compare the results of various studies without standardized measurement methods.

Regardless of the considerations discussed above for strong negative potentials, our Fe- and Ni-N-C catalysts show high CO production rates and *FE* at moderate overpotentials what we assume is attributable to the presence of M-N₄ structures and absence of HER active side phases in our catalysts.⁴⁹ Even though these catalysts show promising product specific current densities (Figure S18) many further aspects such as long term stability, production costs and specific activity of the GDE need to be considered in the future in order to develop M-N-C catalysts that show technologically relevant performances. The model character of the catalysts in this work allows

important conclusions to be drawn about the catalytically active centers in M-N-C catalysts and the results obtained here can provide important impulses for the further development of this catalyst class.

5. Summary

A series of unistructural metal and nitrogen doped carbon (M-N-C) catalysts was synthesized by the pyrolysis and subsequent acid treatment of carbon-supported porphyrins with various central metal ions (Mn^{3+} , Fe^{3+} , Co^{2+} , Ni^{2+} , Cu^{2+} , Zn^{2+} , Sn^{4+}) and investigated for their capabilities to electrochemically reduce CO_2 in aqueous electrolyte. XPS analyses showed that nitrogen and metal species were almost exclusively present as in carbon integrated M-N_4 centers. LSV measurements on GDE, combined with in-line detection of gaseous products, reveal current densities of more than 200 mA cm^{-2} and CO faradaic efficiencies higher than 80 % on Fe-N-C and Ni-N-C catalysts. This is achieved by an almost complete suppression of the HER over a wide potential range. The onset potentials of CO formation at the M-N-C catalysts follow the model of HCOO^* binding energy descriptors on M-N_4 centers, as it is discussed in literature. Sn-N-C was able to majorly produce HCOOH , while the Cu-N-C catalyst produced CH_4 and C_2H_4 with a $FE > 30 \%$ as main products of the CO_2RR . For this catalyst potential-dependent *post mortem* XPS analyses showed that the onset potential of the hydrocarbon formation (ca. -1.5 V (NHE)) can be correlated with a partial reduction of Cu^{2+} to Cu^0 accompanied by a partial demetallation of the Cu-N_4 center. The C_2H_4 formation rate could significantly be enhanced using CO instead of CO_2 as feed gas, indicating that CO might be a key intermediate in the formation of polycarbon-based hydrocarbons. Our work shows, that the simultaneous measurement of current and product formation rates in LSV experiments on M-N-C catalysts with predominantly M-N_4 centers and

similar morphological properties provides valuable insights into the influence of the central metal ion on the potential-dependent CO₂RR behaviour of M-N-C catalysts.

AUTHOR INFORMATION

Corresponding Authors

*E-mail: stephen_daniel.paul@tu-darmstadt.de

*E-Mail: ulrike.kramm@tu-darmstadt.de

*E-Mail: bogdanoff@helmholtz-berlin.de

Acknowledgement

The Darmstadt Graduate School of Excellence Energy Science and Engineering for the GSC 1070 scholarship. This work is co-financed with tax resources on the basis of the tax rate set by the members of the Saxon State Parliament agreed budget. We further thank Charlotte Gallenkamp and Marco Favaro for providing the schematic representations of the M-N-C catalysts in the manuscript and TOC.

Supporting Information

The Supporting Information is available free of charge. It includes

- Experimental details and procedures
- Relevant figures, tables and according explanations as noted in the text (PDF)

Conflict of Interest

The authors declare no conflict of interest

References

(1) Burgess, M. G.; Ritchie, J.; Shapland, J.; Pielke, R. IPCC baseline scenarios have over-projected CO₂ emissions and economic growth. *Environ. Res. Lett.* **2021**, *16*, 14016.

(2) Jacobson, M. Z. Review of solutions to global warming, air pollution, and energy security. *Energy Environ. Sci.* **2009**, *2*, 148–173.

(3) Kauffman, D. R.; Thakkar, J.; Siva, R.; Matranga, C.; Ohodnicki, P. R.; Zeng, C.; Jin, R. Efficient electrochemical CO₂ conversion powered by renewable energy. *ACS applied materials & interfaces* **2015**, *7*, 15626–15632.

(4) Vasileff, A.; Zheng, Y.; Qiao, S. Z. Carbon Solving Carbon's Problems: Recent Progress of Nanostructured Carbon-Based Catalysts for the Electrochemical Reduction of CO₂. *Adv. Energy Mater.* **2017**, *7*, 1700759.

(5) Ganesh, I. Conversion of carbon dioxide into methanol – a potential liquid fuel: Fundamental challenges and opportunities (a review). *Renewable and Sustainable Energy Reviews* **2014**, *31*, 221–257.

(6) Yang, Y.; Tang, Z.; Zhou, B.; Shen, J.; He, H.; Ali, A.; Zhong, Q.; Xiong, Y.; Gao, C.; Alsaedi, A.; Hayat, T.; Wang, X.; Zhou, Y.; Zou, Z. In situ no-slot joint integration of half-metallic C(CN)₃ cocatalyst into g-C₃N₄ scaffold: An absolute metal-free in-plane heterosystem for efficient and selective photoconversion of CO₂ into CO. *Applied Catalysis B: Environmental* **2020**, *264*, 118470.

(7) Hailu, A.; Tamijani, A. A.; Mason, S. E.; Shaw, S. K. Efficient Conversion of CO₂ to Formate Using Inexpensive and Easily Prepared Post-Transition Metal Alloy Catalysts. *Energy Fuels* **2020**, *34*, 3467–3476.

(8) Zhang, T.; Verma, S.; Kim, S.; Fister, T. T.; Kenis, P. J.; Gewirth, A. A. Highly dispersed, single-site copper catalysts for the electroreduction of CO₂ to methane. *Journal of Electroanalytical Chemistry* **2020**, *875*, 113862.

(9) Dong, C.; Ji, M.; Yang, X.; Yao, J.; Chen, H. Reaction Mechanisms of CO₂ Reduction to Formaldehyde Catalyzed by Hourglass Ru, Fe, and Os Complexes: A Density Functional Theory Study. *Catalysts* **2017**, *7*, 5.

(10) Gao, D.; Sinev, I.; Scholten, F.; Arán-Ais, R. M.; Divins, N. J.; Kvashnina, K.; Timoshenko, J.; Roldan Cuenya, B. Selective CO₂ Electroreduction to Ethylene and Multicarbon Alcohols via Electrolyte-Driven Nanostructuring. *Angewandte Chemie (International ed. in English)* **2019**, *58*, 17047–17053.

(11) Yin, Z.; Yu, C.; Zhao, Z.; Guo, X.; Shen, M.; Li, N.; Muzzio, M.; Li, J.; Liu, H.; Lin, H.; Yin, J.; Lu, G.; Su, D.; Sun, S. Cu₃N Nanocubes for Selective Electrochemical Reduction of CO₂ to Ethylene. *Nano letters* **2019**, *19*, 8658–8663.

(12) Aydın, R.; Doğan, H. Ö.; Köleli, F. Electrochemical reduction of carbondioxide on polypyrrole coated copper electro-catalyst under ambient and high pressure in methanol. *Applied Catalysis B: Environmental* **2013**, *140-141*, 478–482.

- (13) Wang, L.; Wei, Y.; Fang, R.; Wang, J.; Yu, X.; Chen, J.; Jing, H. Photoelectrocatalytic CO₂ reduction to ethanol via graphite-supported and functionalized TiO₂ nanowires photocathode. *Journal of Photochemistry and Photobiology A: Chemistry* **2020**, *391*, 112368.
- (14) Hori, Y.; Murata, A.; Takahashi, R. Formation of hydrocarbons in the electrochemical reduction of carbon dioxide at a copper electrode in aqueous solution. *J. Chem. Soc., Faraday Trans. 1* **1989**, *85*, 2309.
- (15) Hori, Y.; Murata, A.; Yoshinami, Y. Adsorption of CO, intermediately formed in electrochemical reduction of CO₂, at a copper electrode. *Faraday Trans.* **1991**, *87*, 125.
- (16) Hori, Y.; Konishi, H.; Futamura, T. A. Murata, O. Koga, H. Sakurai and K. Oguma. *Electrochim. Acta* **2005**, *50*, 5354–5369.
- (17) Li, C. W.; Kanan, M. W. CO₂ reduction at low overpotential on Cu electrodes resulting from the reduction of thick Cu₂O films. *J. Am. Chem. Soc.* **2012**, *134*, 7231–7234.
- (18) Kuhl, K. P.; Cave, E. R.; Abram, D. N.; Jaramillo, T. F. New insights into the electrochemical reduction of carbon dioxide on metallic copper surfaces. *Energy Environ. Sci.* **2012**, *5*, 7050.
- (19) Bagger, A.; Ju, W.; Varela, A. S.; Strasser, P.; Rossmeisl, J. Single site porphyrine-like structures advantages over metals for selective electrochemical CO₂ reduction. *Catalysis Today* **2017**, *288*, 74–78.
- (20) Bhugun, I.; Lexa, D.; Savéant, J.-M. Catalysis of the Electrochemical Reduction of Carbon Dioxide by Iron(0) Porphyrins: Synergistic Effect of Weak Brønsted Acids. *J. Am. Chem. Soc.* **1996**, *118*, 1769–1776.

(21) Birdja, Y. Y.; Shen, J.; Koper, M. T. Influence of the metal center of metalloprotoporphyrins on the electrocatalytic CO₂ reduction to formic acid. *Catalysis Today* **2017**, *288*, 37–47.

(22) Cheng, M.-J.; Kwon, Y.; Head-Gordon, M.; Bell, A. T. Tailoring Metal-Porphyrin-Like Active Sites on Graphene to Improve the Efficiency and Selectivity of Electrochemical CO₂ Reduction. *J. Phys. Chem. C* **2015**, *119*, 21345–21352.

(23) Magdesieva, T. V.; Yamamoto, T.; Tryk, D. A.; Fujishima, A. Electrochemical Reduction of CO₂ with Transition Metal Phthalocyanine and Porphyrin Complexes Supported on Activated Carbon Fibers. *Journal of Electroanalytical Chemistry and Interfacial Electrochemistry* **2002**, *149*, D89.

(24) Shen, J.; Kortlever, R.; Kas, R.; Birdja, Y. Y.; Diaz-Morales, O.; Kwon, Y.; Ledezma-Yanez, I.; Schouten, K. J. P.; Mul, G.; Koper, M. T. M. Electrocatalytic reduction of carbon dioxide to carbon monoxide and methane at an immobilized cobalt protoporphyrin. *Nature communications* **2015**, *6*, 8177.

(25) Tripkovic, V.; Vanin, M.; Karamad, M.; Björketun, M. E.; Jacobsen, K. W.; Thygesen, K. S.; Rossmeisl, J. Electrochemical CO₂ and CO Reduction on Metal-Functionalized Porphyrin-like Graphene. *J. Phys. Chem. C* **2013**, *117*, 9187–9195.

(26) Weng, Z.; Jiang, J.; Wu, Y.; Wu, Z.; Guo, X.; Materna, K. L.; Liu, W.; Batista, V. S.; Brudvig, G. W.; Wang, H. Electrochemical CO₂ Reduction to Hydrocarbons on a Heterogeneous Molecular Cu Catalyst in Aqueous Solution. *J. Am. Chem. Soc.* **2016**, *138*, 8076–8079.

(27) Ren, S.; Joulié, D.; Salvatore, D.; Torbensen, K.; Wang, M.; Robert, M.; Berlinguette, C. P. Molecular electrocatalysts can mediate fast, selective CO₂ reduction in a flow cell. *Science (New York, N.Y.)* **2019**, *365*, 367–369.

(28) Dey, S.; Ahmed, M. E.; Dey, A. Activation of Co(I) State in a Cobalt-Dithiolato Catalyst for Selective and Efficient CO₂ Reduction to CO. *Inorganic Chemistry* **2018**, *57*, 5939–5947.

(29) Torbensen, K.; Joulié, D.; Ren, S.; Wang, M.; Salvatore, D.; Berlinguette, C. P.; Robert, M. Molecular Catalysts Boost the Rate of Electrolytic CO₂ Reduction. *ACS Energy Lett.* **2020**, *5*, 1512–1518.

(30) Varela, A. S.; Ju, W.; Strasser, P. Molecular Nitrogen-Carbon Catalysts, Solid Metal Organic Framework Catalysts, and Solid Metal/Nitrogen-Doped Carbon (MNC) Catalysts for the Electrochemical CO₂ Reduction. *Adv. Energy Mater.* **2018**, *8*, 1703614.

(31) Takeda, H.; Cometto, C.; Ishitani, O.; Robert, M. Electrons, Photons, Protons and Earth-Abundant Metal Complexes for Molecular Catalysis of CO₂ Reduction. *ACS Catal.* **2017**, *7*, 70–88.

(32) Costentin, C.; Robert, M.; Savéant, J.-M. Catalysis of the electrochemical reduction of carbon dioxide. *Chemical Society reviews* **2013**, *42*, 2423–2436.

(33) Manbeck, G. F.; Fujita, E. A review of iron and cobalt porphyrins, phthalocyanines and related complexes for electrochemical and photochemical reduction of carbon dioxide. *J. Porphyrins Phthalocyanines* **2015**, *19*, 45–64.

(34) Schneider, J.; Jia, H.; Muckerman, J. T.; Fujita, E. Thermodynamics and kinetics of CO₂, CO, and H⁺ binding to the metal centre of CO₂ reduction catalysts. *Chemical Society reviews* **2012**, *41*, 2036–2051.

(35) Lin, S.; Diercks, C. S.; Zhang, Y.-B.; Kornienko, N.; Nichols, E. M.; Zhao, Y.; Paris, A. R.; Kim, D.; Yang, P.; Yaghi, O. M.; Chang, C. J. Covalent organic frameworks comprising cobalt porphyrins for catalytic CO₂ reduction in water. *Science (New York, N.Y.)* **2015**, *349*, 1208–1213.

(36) Corbin, N.; Zeng, J.; Williams, K.; Manthiram, K. Heterogeneous molecular catalysts for electrocatalytic CO₂ reduction. *Nano Res.* **2019**, *12*, 2093–2125.

(37) Limburg, B.; Bouwman, E.; Bonnet, S. Molecular water oxidation catalysts based on transition metals and their decomposition pathways. *Coordination Chemistry Reviews* **2012**, *256*, 1451–1467.

(38) Koshy, D. M.; Chen, S.; Lee, D. U.; Stevens, M. B.; Abdellah, A. M.; Dull, S. M.; Chen, G.; Nordlund, D.; Gallo, A.; Hahn, C.; Higgins, D. C.; Bao, Z.; Jaramillo, T. F. Understanding the Origin of Highly Selective CO₂ Electroreduction to CO on Ni,N-doped Carbon Catalysts. *Angewandte Chemie (International ed. in English)* **2020**, *59*, 4043–4050.

(39) Huan, T. N.; Ranjbar, N.; Rouse, G.; Sougrati, M.; Zitolo, A.; Mougél, V.; Jaouen, F.; Fontecave, M. Electrochemical Reduction of CO₂ Catalyzed by Fe-N-C Materials: A Structure–Selectivity Study. *ACS Catal.* **2017**, *7*, 1520–1525.

(40) Khezri, B.; Fisher, A. C.; Pumera, M. CO₂ reduction: the quest for electrocatalytic materials. *J. Mater. Chem. A* **2017**, *5*, 8230–8246.

(41) Leonard, N.; Ju, W.; Sinev, I.; Steinberg, J.; Luo, F.; Varela, A. S.; Roldan Cuenya, B.; Strasser, P. The chemical identity, state and structure of catalytically active centers during the electrochemical CO₂ reduction on porous Fe-nitrogen-carbon (Fe-N-C) materials. *Chemical science* **2018**, *9*, 5064–5073.

(42) Li, X.; Bi, W.; Chen, M.; Sun, Y.; Ju, H.; Yan, W.; Zhu, J.; Wu, X.; Chu, W.; Wu, C.; Xie, Y. Exclusive Ni-N₄ Sites Realize Near-Unity CO Selectivity for Electrochemical CO₂ Reduction. *J. Am. Chem. Soc.* **2017**, *139*, 14889–14892.

(43) Pan, F.; Deng, W.; Justiniano, C.; Li, Y. Identification of champion transition metals centers in metal and nitrogen-codoped carbon catalysts for CO₂ reduction. *Applied Catalysis B: Environmental* **2018**, *226*, 463–472.

(44) Pan, F.; Xiang, X.; Li, Y. Nitrogen Coordinated Single Atomic Metals Supported on Nanocarbons: A New Frontier in Electrocatalytic CO₂ Reduction. *J. Am. Chem. Soc.* **2018**, *29*, 1701784.

(45) Roy, A.; Hursán, D.; Artyushkova, K.; Atanassov, P.; Janáky, C.; Serov, A. Nanostructured metal-N-C electrocatalysts for CO₂ reduction and hydrogen evolution reactions. *Applied Catalysis B: Environmental* **2018**, *232*, 512–520.

(46) Su, P.; Iwase, K.; Nakanishi, S.; Hashimoto, K.; Kamiya, K. Nickel-Nitrogen-Modified Graphene: An Efficient Electrocatalyst for the Reduction of Carbon Dioxide to Carbon Monoxide. *Small (Weinheim an der Bergstrasse, Germany)* **2016**, *12*, 6083–6089.

(47) Varela, A. S.; Ranjbar Sahraie, N.; Steinberg, J.; Ju, W.; Oh, H.-S.; Strasser, P. Metal-Doped Nitrogenated Carbon as an Efficient Catalyst for Direct CO₂ Electroreduction to CO and Hydrocarbons. *Angewandte Chemie (International ed. in English)* **2015**, *54*, 10758–10762.

(48) Zhang, B.; Zhang, J.; Shi, J.; Tan, D.; Liu, L.; Zhang, F.; Lu, C.; Su, Z.; Tan, X.; Cheng, X.; Han, B.; Zheng, L.; Zhang, J. Manganese acting as a high-performance heterogeneous electrocatalyst in carbon dioxide reduction. *Nature communications* **2019**, *10*, 2980.

(49) Varela, A. S.; Ju, W.; Bagger, A.; Franco, P.; Rossmeisl, J.; Strasser, P. Electrochemical Reduction of CO₂ on Metal-Nitrogen-Doped Carbon Catalysts. *ACS Catal.* **2019**, *9*, 7270–7284.

(50) Kramm, U. I.; Herrmann-Geppert, I.; Behrends, J.; Lips, K.; Fiechter, S.; Bogdanoff, P. On an Easy Way To Prepare Metal-Nitrogen Doped Carbon with Exclusive Presence of MeN₄-type Sites Active for the ORR. *J. Am. Chem. Soc.* **2016**, *138*, 635–640.

(51) Kübler, M.; Wagner, S.; Jurzinsky, T.; Paul, S.; Weidler, N.; Gomez Villa, E. D.; Cremers, C.; Kramm, U. I. Impact of Surface Functionalization on the Intrinsic Properties of the Resulting Fe–N–C Catalysts for Fuel Cell Applications. *Energy Technology* **2020**, *8*, 2000433.

(52) Leonard, N. D.; Wagner, S.; Luo, F.; Steinberg, J.; Ju, W.; Weidler, N.; Wang, H.; Kramm, U. I.; Strasser, P. Deconvolution of Utilization, Site Density, and Turnover Frequency of Fe–Nitrogen–Carbon Oxygen Reduction Reaction Catalysts Prepared with Secondary N-Precursors. *ACS Catal.* **2018**, *8*, 1640–1647.

(53) Kramm, U. I.; Herrmann-Geppert, I.; Bogdanoff, P.; Fiechter, S. Effect of an Ammonia Treatment on Structure, Composition, and Oxygen Reduction Reaction Activity of Fe–N–C Catalysts. *J. Phys. Chem. C* **2011**, *115*, 23417–23427.

(54) Kramm, U. I.; Lefèvre, M.; Larouche, N.; Schmeisser, D.; Dodelet, J.-P. Correlations between mass activity and physicochemical properties of Fe/N/C catalysts for the ORR in PEM fuel cell via ^{57}Fe Mössbauer spectroscopy and other techniques. *J. Am. Chem. Soc.* **2014**, *136*, 978–985.

(55) Zitolo, A.; Goellner, V.; Armel, V.; Sougrati, M.-T.; Mineva, T.; Stievano, L.; Fonda, E.; Jaouen, F. Identification of catalytic sites for oxygen reduction in iron- and nitrogen-doped graphene materials. *Nature materials* **2015**, *14*, 937–942.

(56) Jiang, J.; Luo, R.; Zhou, X.; Chen, Y.; Ji, H. Photocatalytic Properties and Mechanistic Insights into Visible Light-Promoted Aerobic Oxidation of Sulfides to Sulfoxides via Tin Porphyrin-Based Porous Aromatic Frameworks. *Adv. Synth. Catal.* **2018**, *360*, 4402–4411.

(57) Wu, J.; Liu, M.; Sharma, P. P.; Yadav, R. M.; Ma, L.; Yang, Y.; Zou, X.; Zhou, X.-D.; Vajtai, R.; Yakobson, B. I.; Lou, J.; Ajayan, P. M. Incorporation of Nitrogen Defects for Efficient Reduction of CO_2 via Two-Electron Pathway on Three-Dimensional Graphene Foam. *Nano letters* **2016**, *16*, 466–470.

(58) Jiao, Y.; Zheng, Y.; Chen, P.; Jaroniec, M.; Qiao, S.-Z. Molecular Scaffolding Strategy with Synergistic Active Centers To Facilitate Electrocatalytic CO_2 Reduction to Hydrocarbon/Alcohol. *J. Am. Chem. Soc.* **2017**, *139*, 18093–18100.

(59) Yang, L.; Larouche, N.; Chenitz, R.; Zhang, G.; Lefèvre, M.; Dodelet, J.-P. Activity, Performance, and Durability for the Reduction of Oxygen in PEM Fuel Cells, of Fe/N/C Electrocatalysts Obtained from the Pyrolysis of Metal-Organic-Framework and Iron Porphyrin Precursors. *Electrochimica Acta* **2015**, *159*, 184–197.

(60) Jiang, K.; Siahrostami, S.; Akey, A. J.; Li, Y.; Lu, Z.; Lattimer, J.; Hu, Y.; Stokes, C.; Gangishetty, M.; Chen, G.; Zhou, Y.; Hill, W.; Cai, W.-B.; Bell, D.; Chan, K.; Nørskov, J. K.; Cui, Y.; Wang, H. Transition-Metal Single Atoms in a Graphene Shell as Active Centers for Highly Efficient Artificial Photosynthesis. *Chem* **2017**, *3*, 950–960.

(61) Zhu, G.; Li, Y.; Zhu, H.; Su, H.; Chan, S. H.; Sun, Q. Curvature-Dependent Selectivity of CO₂ Electrocatalytic Reduction on Cobalt Porphyrin Nanotubes. *ACS Catal.* **2016**, *6*, 6294–6301.

(62) Weng, Z.; Wu, Y.; Wang, M.; Jiang, J.; Yang, K.; Huo, S.; Wang, X.-F.; Ma, Q.; Brudvig, G. W.; Batista, V. S.; Liang, Y.; Feng, Z.; Wang, H. Active sites of copper-complex catalytic materials for electrochemical carbon dioxide reduction. *Nature communications* **2018**, *9*, 415.

(63) Karapinar, D.; Huan, N. T.; Ranjbar Sahraie, N.; Li, J.; Wakerley, D.; Touati, N.; Zanna, S.; Taverna, D.; Galvão Tizei, L. H.; Zitolo, A.; Jaouen, F.; Mougél, V.; Fontecave, M. Electroreduction of CO₂ on Single-Site Copper-Nitrogen-Doped Carbon Material: Selective Formation of Ethanol and Reversible Restructuration of the Metal Sites. *Angew. Chem.* **2019**, *131*, 15242–15247.

(64) Kramm, U. I.; Abs-Wurmbach, I.; Fiechter, S.; Herrmann, I.; Radnik, J.; Bogdanoff, P. New Insight into the Nature of Catalytic Activity of Pyrolysed Iron Porphyrin Based Electro-Catalysts for the Oxygen Reduction Reaction (ORR) in Acidic Media. *ECS Trans.* **2009**, *25*, 93–104.

(65) Varela, A. S.; Kroschel, M.; Leonard, N. D.; Ju, W.; Steinberg, J.; Bagger, A.; Rossmeisl, J.; Strasser, P. pH Effects on the Selectivity of the Electrocatalytic CO₂ Reduction on Graphene-Embedded Fe–N–C Motifs: Bridging Concepts between Molecular Homogeneous and Solid-State Heterogeneous Catalysis. *ACS Energy Lett.* **2018**, *3*, 812–817.

- (66) Bogdanoff, P.; Herrmann, I.; Hilgendorff, M.; Dorbandt, I.; Fiechter, S.; Tributsch, H. Probing structural effects of pyrolysed CoTMPP-based electrocatalysts for oxygen reduction via new preparation strategies. *Journal of new materials for electrochemical systems* **2004**, *7*, 85–92.
- (67) Kramm, U. I.; Abs-Wurmbach, I.; Herrmann-Geppert, I.; Radnik, J.; Fiechter, S.; Bogdanoff, P. Influence of the Electron-Density of FeN₄-Centers Towards the Catalytic Activity of Pyrolyzed FeTMPPCl-Based ORR-Electrocatalysts. *J. Electrochem. Soc.* **2011**, *158*, B69.
- (68) Widelöv, A. Pyrolysis of iron and cobalt porphyrins sublimated onto the surface of carbon black as a method to prepare catalysts for O₂ reduction. *Electrochimica Acta* **1993**, *38*, 2493–2502.
- (69) Yeager, E. Electrocatalysis on non-metallic surfaces. *NBS Special Publication* **1976**, *455*, 203.
- (70) Karweik, D. H.; Winograd, N. Nitrogen charge distributions in free-base porphyrins, metalloporphyrins, and their reduced analogs observed by X-ray photoelectron spectroscopy. *Inorganic Chemistry* **1976**, *15*, 2336–2342.
- (71) Canesson, P.; Cruz, M. I.; van Damme, H. X.P.S. Study of the Interaction of Some Porphyrins and Metalloporphyrins with Montmorillonite. *Development in sedimentology* **1979**, *27*, 217–225.
- (72) Scherson, D.; Tanaka, A. A.; Gupta, S. L.; Tryk, D.; Fierro, C.; Holze, R.; Yeager, E. B.; Lattimer, R. P. Transition metal macrocycles supported on high area carbon: Pyrolysis-mass spectrometry studies. *Electrochimica Acta* **1986**, *31*, 1247–1258.

(73) Ikeda, O.; Fukuda, H.; Tamura, H. The effect of heat treatment on group VIII B porphyrins as electrocatalysts in the cathodic reduction of oxygen. *J. Chem. Soc., Faraday Trans. 1* **1986**, *82*, 1561.

(74) Artyushkova, K.; Levendosky, S.; Atanassov, P.; Fulghum, J. XPS Structural Studies of Nano-composite Non-platinum Electrocatalysts for Polymer Electrolyte Fuel Cells. *Top Catal* **2007**, *46*, 263–275.

(75) Carniato, S.; Roulet, H.; Dufour, G.; Palacin, S.; Barraud, A.; Millié, P.; Nenner, I. Electronic structure of nitrogen square planar copper complexes in Langmuir-Blodgett films. *The Journal of physical chemistry* **1992**, *96*, 7072–7075.

(76) Mele, G.; Del Sole, R.; Vasapollo, G.; Marci, G.; García-Lopez, E.; Palmisano, L.; Coronado, J. M.; Hernández-Alonso, M. D.; Malitesta, C.; Guascito, M. R. TRMC, XPS, and EPR characterizations of polycrystalline TiO₂ porphyrin impregnated powders and their catalytic activity for 4-nitrophenol photodegradation in aqueous suspension. *J. Phys. Chem. B* **2005**, *109*, 12347–12352.

(77) Killian, M. S.; Gnichwitz, J.-F.; Hirsch, A.; Schmuki, P.; Kunze, J. ToF-SIMS and XPS studies of the adsorption characteristics of a Zn-porphyrin on TiO₂. *Langmuir: the ACS journal of surfaces and colloids* **2010**, *26*, 3531–3538.

(78) Kaplan, A.; Korin, E.; Bettelheim, A. Structures Self-Assembled from Anionic Graphene and Cationic Manganese Porphyrin: Characterization and Application in Artificial Photosynthesis. *Eur. J. Inorg. Chem.* **2014**, *2014*, 2288–2295.

(79) Gojković, S. L.; Gupta, S.; Savinell, R. F. Heat-Treated Iron(III) Tetramethoxyphenyl Porphyrin Supported on High-Area Carbon as an Electrocatalyst for Oxygen Reduction: I. Characterization of the Electrocatalyst. *J. Electrochem. Soc.* **1998**, *145*, 3493–3499.

(80) Luo, F.; Roy, A.; Silvioli, L.; Cullen, D. A.; Zitolo, A.; Sougrati, M. T.; Oguz, I. C.; Mineva, T.; Teschner, D.; Wagner, S.; Wen, J.; Dionigi, F.; Kramm, U. I.; Rossmeisl, J.; Jaouen, F.; Strasser, P. P-block single-metal-site tin/nitrogen-doped carbon fuel cell cathode catalyst for oxygen reduction reaction. *Nature materials* **2020**, *19*, 1215–1223.

(81) Sun, Y.; Silvioli, L.; Sahraie, N. R.; Ju, W.; Li, J.; Zitolo, A.; Li, S.; Bagger, A.; Arnarson, L.; Wang, X.; Moeller, T.; Bernsmeier, D.; Rossmeisl, J.; Jaouen, F.; Strasser, P. Activity-Selectivity Trends in the Electrochemical Production of Hydrogen Peroxide over Single-Site Metal-Nitrogen-Carbon Catalysts. *J. Am. Chem. Soc.* **2019**, *141*, 12372–12381.

(82) Zhang, Z.; Xiao, J.; Chen, X.-J.; Yu, S.; Yu, L.; Si, R.; Wang, Y.; Wang, S.; Meng, X.; Wang, Y.; Tian, Z.-Q.; Deng, D. Reaction Mechanisms of Well-Defined Metal-N₄ Sites in Electrocatalytic CO₂ Reduction. *Angewandte Chemie (International ed. in English)* **2018**, *57*, 16339–16342.

(83) Koslowski, U. I.; Abs-Wurmbach, I.; Fiechter, S.; Bogdanoff, P. Nature of the Catalytic Centers of Porphyrin-Based Electrocatalysts for the ORR: A Correlation of Kinetic Current Density with the Site Density of Fe–N₄ Centers. *J. Phys. Chem. C* **2008**, *112*, 15356–15366.

(84) Herrmann, I.; Kramm, U. I.; Fiechter, S.; Bogdanoff, P. Oxalate supported pyrolysis of CoTMPP as electrocatalysts for the oxygen reduction reaction. *Electrochimica Acta* **2009**, *54*, 4275–4287.

(85) Burdyny, T.; Smith, W. A. CO₂ reduction on gas-diffusion electrodes and why catalytic performance must be assessed at commercially-relevant conditions. *Energy Environ. Sci.* **2019**, *12*, 1442–1453.

(86) Verma, S.; Lu, X.; Ma, S.; Masel, R. I.; Kenis, P. J. A. The effect of electrolyte composition on the electroreduction of CO₂ to CO on Ag based gas diffusion electrodes. *Physical chemistry chemical physics: PCCP* **2016**, *18*, 7075–7084.

(87) Möller, T.; Ju, W.; Bagger, A.; Wang, X.; Luo, F.; Ngo Thanh, T.; Varela, A. S.; Rossmeisl, J.; Strasser, P. Efficient CO₂ to CO electrolysis on solid Ni–N–C catalysts at industrial current densities. *Energy Environ. Sci.* **2019**, *12*, 640–647.

(88) Ju, W.; Bagger, A.; Wang, X.; Tsai, Y.; Luo, F.; Möller, T.; Wang, H.; Rossmeisl, J.; Varela, A. S.; Strasser, P. Unraveling Mechanistic Reaction Pathways of the Electrochemical CO₂ Reduction on Fe–N–C Single-Site Catalysts. *ACS Energy Lett.* **2019**, *4*, 1663–1671.

(89) Wang, L.; Nitopi, S. A.; Bertheussen, E.; Orazov, M.; Morales-Guio, C. G.; Liu, X.; Higgins, D. C.; Chan, K.; Nørskov, J. K.; Hahn, C.; Jaramillo, T. F. Electrochemical Carbon Monoxide Reduction on Polycrystalline Copper: Effects of Potential, Pressure, and pH on Selectivity toward Multicarbon and Oxygenated Products. *ACS Catal.* **2018**, *8*, 7445–7454.

(90) Wang, X.; Araújo, J. F. de; Ju, W.; Bagger, A.; Schmies, H.; Kühl, S.; Rossmeisl, J.; Strasser, P. Mechanistic reaction pathways of enhanced ethylene yields during electroreduction of CO₂-CO co-feeds on Cu and Cu-tandem electrocatalysts. *Nature nanotechnology* **2019**, *14*, 1063–1070.

(91) Nitopi, S.; Bertheussen, E.; Scott, S. B.; Liu, X.; Engstfeld, A. K.; Horch, S.; Seger, B.; Stephens, I. E. L.; Chan, K.; Hahn, C.; Nørskov, J. K.; Jaramillo, T. F.; Chorkendorff, I. Progress and Perspectives of Electrochemical CO₂ Reduction on Copper in Aqueous Electrolyte. *Chemical reviews* **2019**, *119*, 7610–7672.

(92) Baturina, O. A.; Lu, Q.; Padilla, M. A.; Le Xin; Li, W.; Serov, A.; Artyushkova, K.; Atanassov, P.; Xu, F.; Epshteyn, A.; Brintlinger, T.; Schuette, M.; Collins, G. E. CO₂ Electroreduction to Hydrocarbons on Carbon-Supported Cu Nanoparticles. *ACS Catal.* **2014**, *4*, 3682–3695.

(93) Guascito, M. R.; Ricciardi, G.; Rosa, A. Nickel-macrocycle interaction in nickel(II) porphyrins and porphyrazines bearing alkylthio β-substituents: A combined DFT and XPS study. *J. Porphyrins Phthalocyanines* **2017**, *21*, 371–380.

(94) Ju, W.; Bagger, A.; Hao, G.-P.; Varela, A. S.; Sinev, I.; Bon, V.; Roldan Cuenya, B.; Kaskel, S.; Rossmeisl, J.; Strasser, P. Understanding activity and selectivity of metal-nitrogen-doped carbon catalysts for electrochemical reduction of CO₂. *Nature communications* **2017**, *8*, 944.

(95) Shi, J.-J.; Hu, X.-M.; Madsen, M. R.; Lamagni, P.; Bjerglund, E. T.; Pedersen, S. U.; Skrydstrup, T.; Daasbjerg, K. Facile Synthesis of Iron- and Nitrogen-Doped Porous Carbon for Selective CO₂ Electroreduction. *ACS Appl. Nano Mater.* **2018**, *1*, 3608–3615.

(96) Yang, F.; Song, P.; Liu, X.; Mei, B.; Xing, W.; Jiang, Z.; Gu, L.; Xu, W. Highly Efficient CO₂ Electroreduction on ZnN₄-based Single-Atom Catalyst. *Angewandte Chemie (International ed. in English)* **2018**, *57*, 12303–12307.